Heterostructured Cobalt Silicide Nanocrystals: Synthesis in Molten Salts, Ferromagnetism, and Electrocatalysis

Yang Song, Isabel Gómez-Recio, Anissa Ghoridi, Fernando Igoa Saldaña, Daniel Janisch, Capucine Sassoye, Vincent Dupuis, David Hrabovsky, M. Luisa Ruiz-González, José González-Calbet, et al.

Heterostructured cobalt silicide nanocrystals: synthesis in molten salts, ferromagnetism and electrocatalysis

Yang Song,[a] Isabel Gómez-Recio,[a] Anissa Ghoridi,[a] Fernando Igoa Saldaña,[a] Daniel Janisch,[a] Capucine Sassoye,[a] Vincent Dupuis,[b] David Hrabovsky,[c] M. Luisa Ruiz-González,[d] José M. González-Calbet,[d] Sandra Casale,[e] Andrea Zitolo,[f] Benedikt Lassalle-Kaiser,[f] Christel Laberty-Robert,[a] David Portehault[a,*]

[a] Sorbonne Université, CNRS, Laboratoire de Chimie de la Matière Condensée de Paris (CMCP), 4 place Jussieu, F-75005, Paris, France

[b] Sorbonne Université, CNRS, Laboratoire de Physicochimie des Electrolytes et Nanosystèmes Interfaciaux (PHENIX), 4 place Jussieu, F-75005, Paris, France

[c] Sorbonne Université, CNRS, Institut de Minéralogie de Physique des Matériaux et de Cosmochimie (IMPMC), 4 place Jussieu, F-75005, Paris, France

[d] Dpto. de Química Inorgánica I, Facultad de Ciencias Químicas, Universidad Complutense, 28040 Madrid, Spain

[e] Sorbonne Université, CNRS, Laboratoire de Réactivité de Surface (LRS), 4 place Jussieu, F-75005, Paris, France

[f] Synchrotron SOLEIL, L'Orme des Merisiers, Départementale 128, 91190 Saint-Aubin, France

Corresponding author: david.portehault@sorbonne-universite.fr

ABSTRACT

Nanoscale heterostructures of covalent intermetallics should give birth to a wide range of interface-driven physical and chemical properties. Such a level of design however remains unattainable for most of these compounds, due to the difficulty to reach a crystalline order of covalent bonds at the moderate temperatures required for colloidal chemistry. Herein we design heterostructured cobalt silicide nanoparticles to trigger magnetic and catalytic properties in silicon-based materials. Our strategy consists in controlling the diffusion of cobalt atoms into silicon nanoparticles, by reacting these particles in molten salts. By adjusting the temperature, we tune the conversion of the initial silicon particles towards homogeneous CoSi nanoparticles and core-shell nanoparticles made of a CoSi shell and a silicon-rich core. The increased interface-to-volume ratio of the CoSi component in the core-shell particles yields distinct properties compared to the bulk and to homogeneous nanoparticles. First, the core-shell particles exhibit increased ferromagnetism, despite the bulk diamagnetic properties of cobalt monosilicide. Second, the core-shell nanoparticles act as efficient pre-catalysts for alkaline water oxidation, where the nanostructure is converted *in situ* into a layered cobalt silicon oxide/(oxy)hydroxide with high and stable OER electrocatalytic activity. This work demonstrates a route to design heterostructured nanocrystals of covalent intermetallic compounds and shows that these new structures exhibit very rich, yet poorly explored, interface-based physical properties and reactivity.

INTRODUCTION

Heterostructured nanoparticles provide distinct properties of large interest for many applications like optoelectronics and catalysis.[1,2] While the design of such nano-objects has reached an exquisite control for metals, oxides and chalcogenides,[1,2] it has not been achieved yet for intermetallics that require high synthesis temperatures, especially those bearing significant covalence in their bonding scheme.

Transition metal silicides are intermetallic compounds showing diverse properties for microelectronics,[3] thermoelectrics,[4] superconductivity,[5] magnetism,[6–9] and (electro)catalysis[10–14]. These properties are deeply impacted by the nanoscale. For instance, unusual ferromagnetism has been observed in nanowires of binary disilicides and monosilicides,[8,9] like cobalt silicide CoSi, as a result of crystal defects, undercoordinated metal atoms and dangling bonds at interfaces.[7] Some silicides like CoSi are also topological semimetals at the surface of which new transport and physical phenomena emerge.[15,16] However the role of the shape and of the internal structure of silicide nano-objects on their magnetic properties has not been examined because of the scarcity of synthesis methods for silicide nanoparticles.[10,12,17] Nanoscaled metal silicides have also raised interest in hydrogenation catalysis[13] and electrocatalysis of the hydrogen evolution and oxygen evolution reactions (HER and OER) involved in water splitting.[10,12,14] Other compounds of p-block elements are attractive for electrochemical water splitting, especially cobalt-p-block element compounds like carbides, nitrides, phosphides, sulfides and borides as pre-catalysts for OER:[18–24] During OER electrocatalysis, they undergo surface reconstruction into electrocatalytically active cobalt (oxy)hydroxides, thus yielding highly active electrocatalysts. Cobalt silicide nanoparticles are a missing piece in this compendium, which relates directly to the challenge raised by their synthesis.

CoSi nanowires[8] and nanoparticles[25–29] are currently achievable by chemical vapor deposition (CVD) at ca. 800-1000 °C. A consequence of CVD growth is that these objects are usually supported on graphene or other substrates. These supports can deeply impact magnetic and catalytic properties of the nano-objects.[30] Altogether, designing freestanding CoSi nanoparticles with tunable surface states should provide original insights into the role of shape and interfaces on the magnetic and electrocatalytic properties of silicides, and should bring the ability to control these properties. However, the synthesis temperature must be drastically decreased compared to the aforementioned CVD processes in order to isolate nanoparticles.

In this work, we bypass the current temperature threshold of cobalt monosilicide synthesis by controlling the diffusion of cobalt atoms into Si nanoparticles dispersed in molten salts, to design freestanding core-shell and homogeneous cobalt silicide nanoparticles (**Figure 1**). The development of nanoparticles exempt of any support with adjustable internal heterostructure provides the unique opportunity to address the role of interfaces on the magnetic and electrocatalytic properties of cobalt monosilicide.

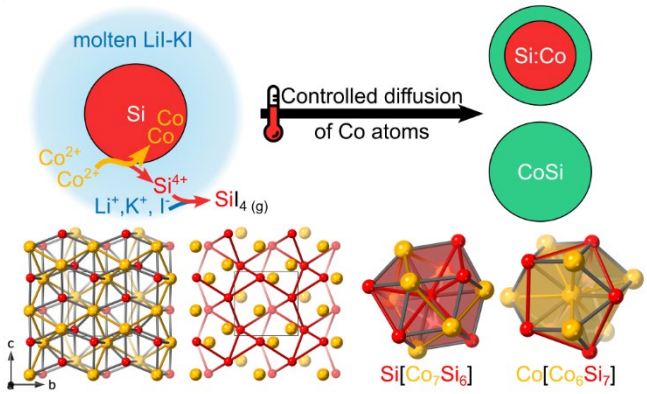

Figure 1. Reaction pathway towards CoSi nanoparticles and the corresponding crystal structure. The coordination polyhedral of Si and Co are shown. Yellow, grey and red bonds display Co-Co, Co-Si and Si-Si bonds.

RESULTS AND DISCUSSION

To achieve a dramatic decrease in the temperature of reaction between silicon and cobalt chloride compared to CVD,[8] we use silicon nanoparticles (diamond-like structure d-Si, ca. 40 nm) (**Figure S1**) and cobalt chloride as Si and Co sources, respectively. Silicon nanoparticles provide a large reaction interface. We perform the reaction in the LiI-KI eutectic mixture (melting point 286 °C), which provides a diluted and carbon-free reaction medium stable at 300-400 °C, thus enabling to increase the reagents mobility, enhance reaction rates and trigger extensive nucleation.[31] Besides, we use dynamic vacuum in order to extract the side-product SiI_4 during the reaction.

Design of homogeneous and core-shell silicide nanoparticles

Powder X-ray diffraction (XRD, **Figure S2**) indicates that CoSi (S.G. $P2_13$) is the main crystalline phase for samples synthesized at 300 and 400 °C. d-Si is still detected in the sample obtained at 300 °C, showing that the silicon nanoparticles are not totally converted at this temperature. Transmission electron microscopy (TEM, **Figure S2** and **Figure 2**) shows that the 400 °C sample is made of homogeneous 20-50 nm nanoparticles. High resolution TEM (HRTEM, **Figure 2**) images, the corresponding Fast Fourier Transforms (FFTs), and scanning TEM (STEM) coupled to high angle annular dark field (HAADF) detection (**Figure 3**) can all be indexed along the CoSi structure (**Figure 1** and **Figure S3**) and confirm that these homogeneous nanoparticles are solely made of CoSi. Some zone axes yield composite atom columns made of Co and Si atoms piled together (**Figure S3**), which can be detected from a brighter HAADF contrast of these columns compared to Si-only columns (**Figure 3c,e-f**). Complementary STEM imaging in annular bright field mode (STEM-ABF) sensitive to light elements (**Figure S4**) confirms the Si distribution, as well as the chemical maps acquired by electron energy loss spectrocopy (EELS, **Figure 3g-l**).

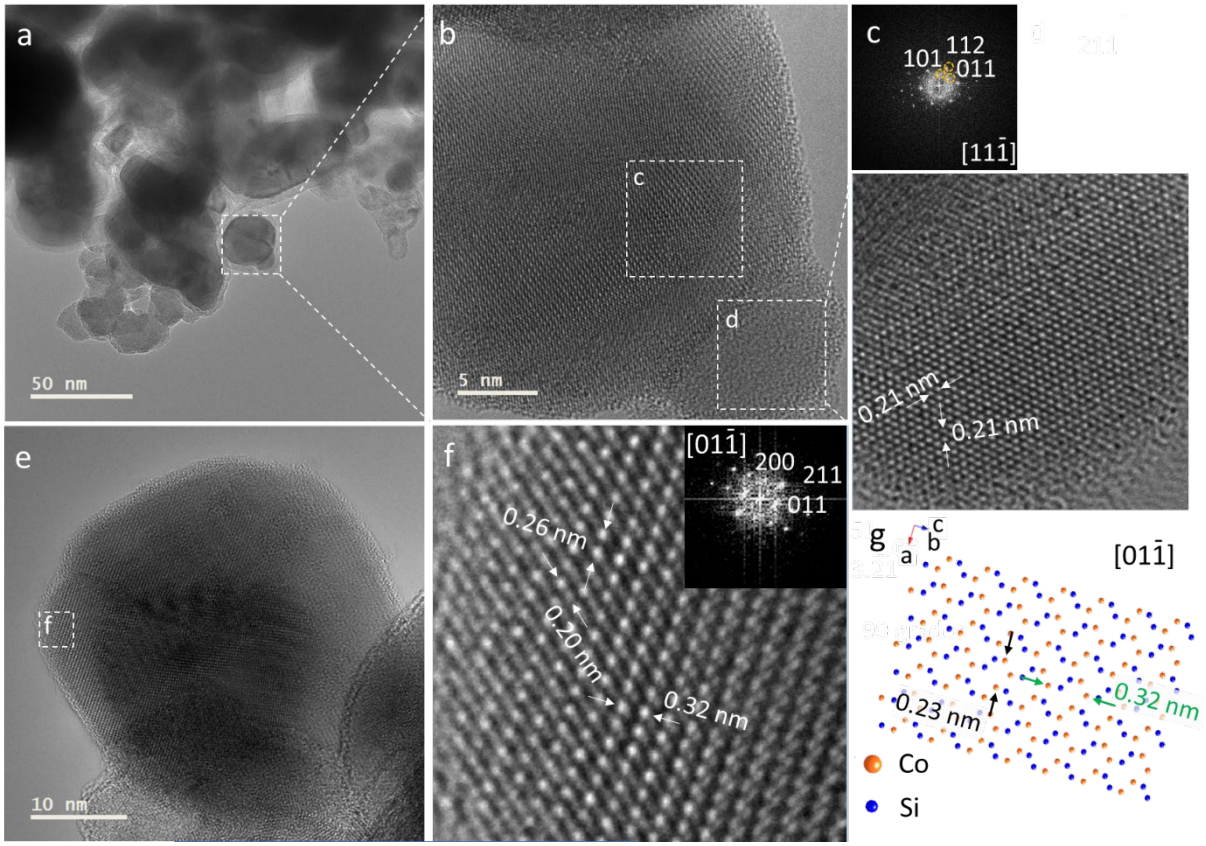

Figure 2. Homogeneous CoSi nanoparticles obtained at 400 °C. (a, e) Low and (b, f) high resolution TEM images with (c, d) corresponding FFTs, indexed along the CoSi structure. (g) Scheme of the CoSi structure with similar orientation as the (f) panel.

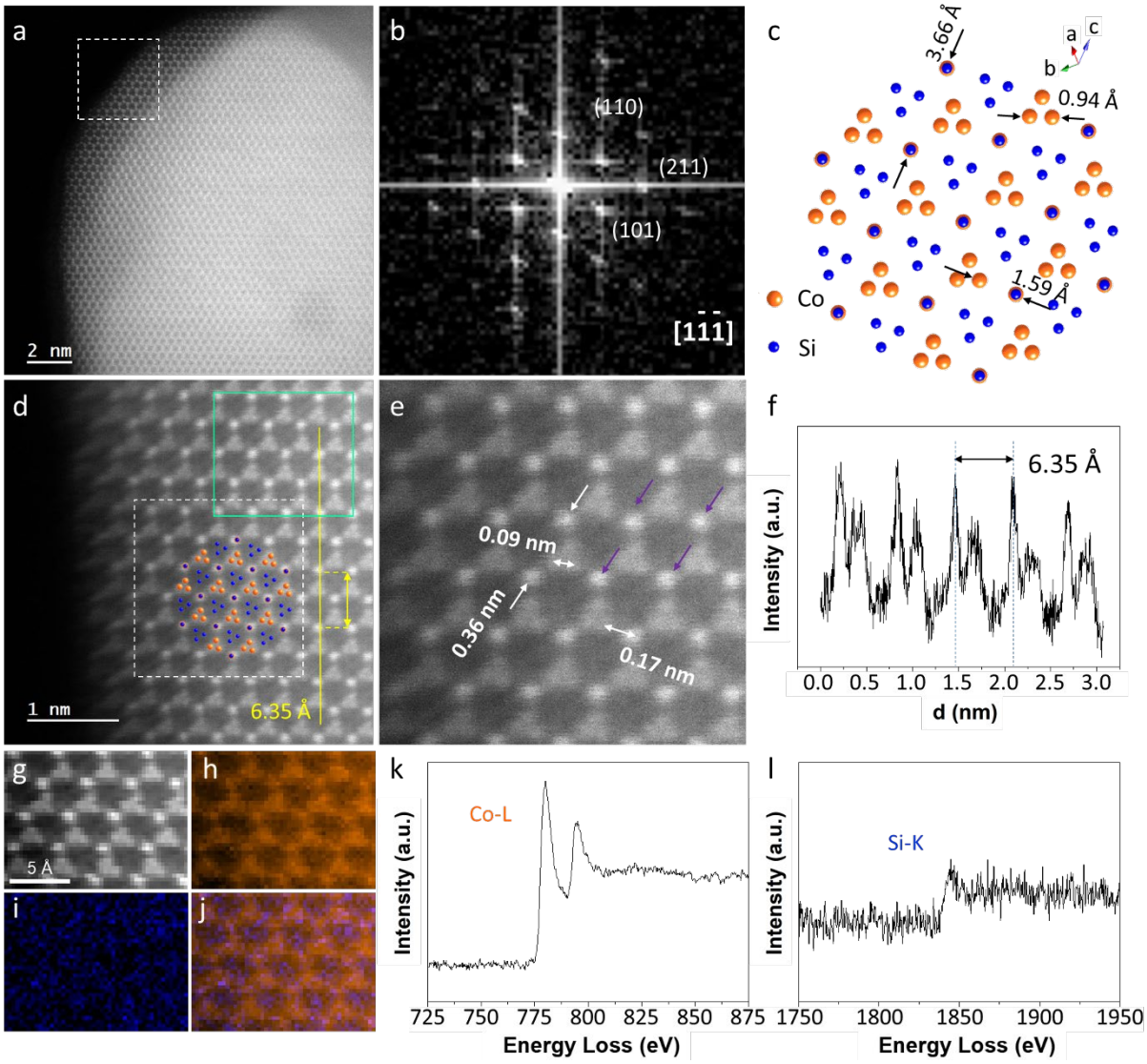

Figure 3. Structural and compositional analysis of homogeneous CoSi nanoparticles. (a) STEM-HAADF image and (b) corresponding FFT of the dashed labelled region. (d, e) STEM-HAADF images ((e) corresponds to the dashed square in (d)). A scheme of the CoSi structure oriented along the [1$\bar{1}\bar{1}$] direction is plotted in (c) and superimposed to the image in (d). (f) Contrast intensity profile along the yellow line displayed on (d). (g) STEM-HAADF image simultaneously acquired with (h) Co-L and (i) Si-K chemical maps on the green area in (d). (j) shows the combined Co and Si maps. EELS sum spectra of Co-L and Si-K edges are displayed in (k) and (l), respectively. (h-j) are displayed at the same scale as (g).

When the synthesis temperature is decreased to 300 °C, then the 20-50 nm nanoparticles exhibit a core-shell structure, highlighted by STEM-HAADF (**Figure 4a-b**) and STEM-ABF (**Figure 4c**), contrary to the homogeneous particles obtained at 400 °C. STEM-HAADF (**Figure 4d**) is consistent with the CoSi structure. HRTEM (**Figure S5**) indicates that the

~5 nm-thick shell is crystallized along the CoSi structure, with crystal domains of 2-5 nm, smaller than the crystal domains of the homogeneous particles (10-15 nm, **Figure 2b-f**, **Figure 3a**). Some domains in the core could be indexed along the d-Si structure according to HRTEM (**Figure S5**). We have then further assessed the spatial distribution of Co and Si by STEM coupled to energy dispersive X-ray spectroscopy (STEM-EDS) and by STEM-EELS (**Figure 4g-l**). The contrasted shell is enriched in cobalt as expected from its CoSi structure. On the opposite, the core is silicon-rich. Note however that we still detect cobalt in the core of the particles. Although it may arise from the top and bottom CoSi shell that is inevitably probed when analyzing the core, we do not discard the possibility of some cobalt atoms in the core, despite the detection of d-Si structure domains, which may suggest cobalt-doped silicon in the core. We then suggest that the core-shell nanoparticles are made of cobalt-doped silicon cores (Si:Co) and CoSi shells. As expected, this inhomogeneity is not observed in homogeneous CoSi nanoparticles. We also observe for both kinds of particles a poorly-contrasted passivation layer rich in silicon and oxygen (**Figure 4g-l**). This layer is more clearly detected by TEM and STEM-ABF **(Figures S5** and **4c**) than by STEM-HAADF (see *e.g.* **Figure 3a**), which confirms its constitution from light elements. We note that this layer is also thicker when the time of air exposure increases (few minutes for **Figure 2** *versus* few days for **Figure S5**), which indicates its formation through a passivation mechanism. We further address more in-depth the exact nature of this outer layer.

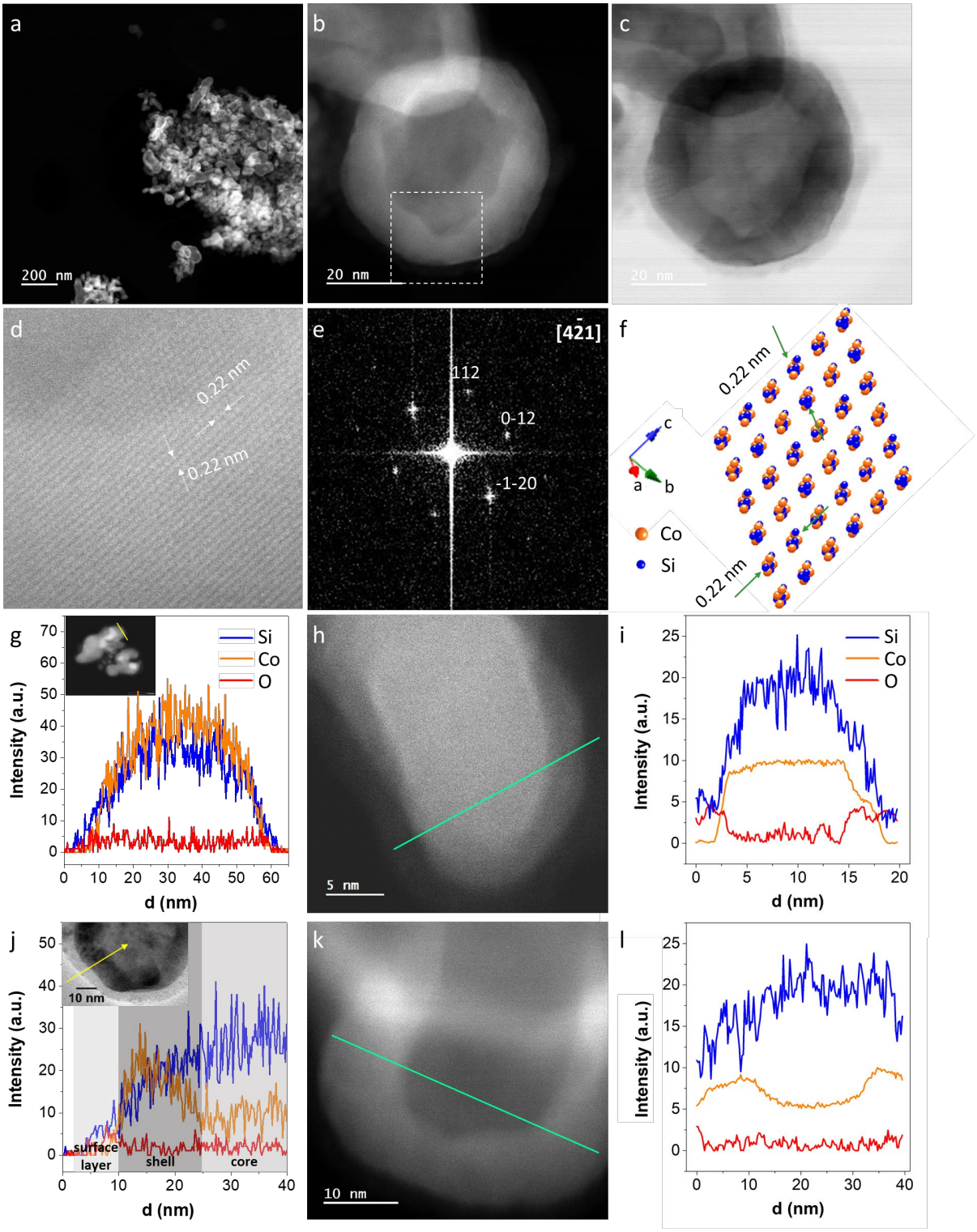

Figure 4. Structure and composition of core-shell nanoparticles. (a, b) STEM-HAADF and (c) STEM-ABF images. (d) Enlarged image of the dashed region in (b), with the corresponding (e) FFT indexed along the CoSi unit cell and (f) the CoSi structure oriented along the same zone axis. STEM-EDS linear profiles along the lines indicated in the insets, STEM-HAADF images and corresponding EELS linear profiles for (g, h, i) homogeneous and (j, k, l) core-shell nanoparticles, respectively.

The evolution from original silicon nanoparticles to Si:Co-CoSi core-shell and then to CoSi homogeneous particles upon an increase of the synthesis temperature, while maintaining the overall particle size suggests a conversion of the initial Si particles by thermally activated diffusion of Co atoms into the Si lattice.[32] This interpretation is supported by the fact that some of the smallest particles at 300 °C are fully converted into CoSi (**Figure S6**), in agreement with the shorter Co diffusion length required for their transformation. Consistently, HRTEM images confirm larger crystal domains in homogeneous CoSi nanoparticles obtained at 400 °C (12-30 nm, **Figure 2**), than for the core-shell nanoparticles at 300 °C (4-8 nm, **Figure S6**).

We then performed STEM-EELS analysis (**Figures S7 and S8**) to address the electronic state of cobalt and silicon into the homogeneous and core-shell nanoparticles. Into both kinds of particles, the Co-L edge does not show features of oxidized cobalt like a L_3 high energy tail (**Figure S9**),[33,34] which suggests cobalt in the metallic state. This is confirmed by the integration of EEL spectra over 1 nm-thick layers from the surface to the core in a homogeneous particle (**Figure 5a-d**). X-ray absorption spectra at the Co-K edge (**Figure 5e**) are identical for both homogeneous and core-shell nanoparticles. They do not exhibit any feature of the reference spectra of oxidized Co species. These spectra confirm that cobalt is in its metallic state, as expected for an intermetallic compound, with no indication of oxidized cobalt. Likewise, the XANES of the Si K-edge shows a main contribution of non-oxidic silicon. A second contribution of oxidic Si is observed with a peak at 1847 eV, in agreement with the EELS Si K- (**Figure S7c-d** and **S8c-d**), Co K- and O K-edges (**Figure 5c**) indicating an outer 0.5 nm-thick passivation layer made of oxygen and silicon. X-ray photoelectron spectroscopy (XPS) (**Figure S10**) indicates the expected contributions of the cobalt silicide, with also some oxidized silicon and cobalt, formed by air exposure. Overall, TEM, STEM-ABF **(Figures S5** and **4c**), STEM-HAADF (**Figure 3a**) and STEM-EELS (**Figure S7c-d** and **S8c-d**) indicate that the amorphous layer is amorphous silica. The detection of oxidized Co by XPS may be ascribed to

extensive oxidation during exposure to air for several days before measurement. This hypothesis is supported by three analyses: the thickening of the amorphous layer upon exposure to air observed by TEM (*vide supra*), the absence of paramagnetic species detected when the samples are handled and studied under inert atmosphere, and Extended X-ray Absorption Fine Structure (EXAFS). Indeed, the Co K-edge EXAFS analysis for the homogeneous CoSi nanoparticles measured after exposure to air for only few minutes fits with an excellent agreement to the crystallographic structure of CoSi (**Figure S11** and **Table S1**). These three evidences show that Co in the homogeneous CoSi nanoparticle sample is present only in the CoSi structure. This material can then be used as CoSi reference for further analysis of the Co K-edge XAS acquired during electrocatalysis, as will be discussed latter.

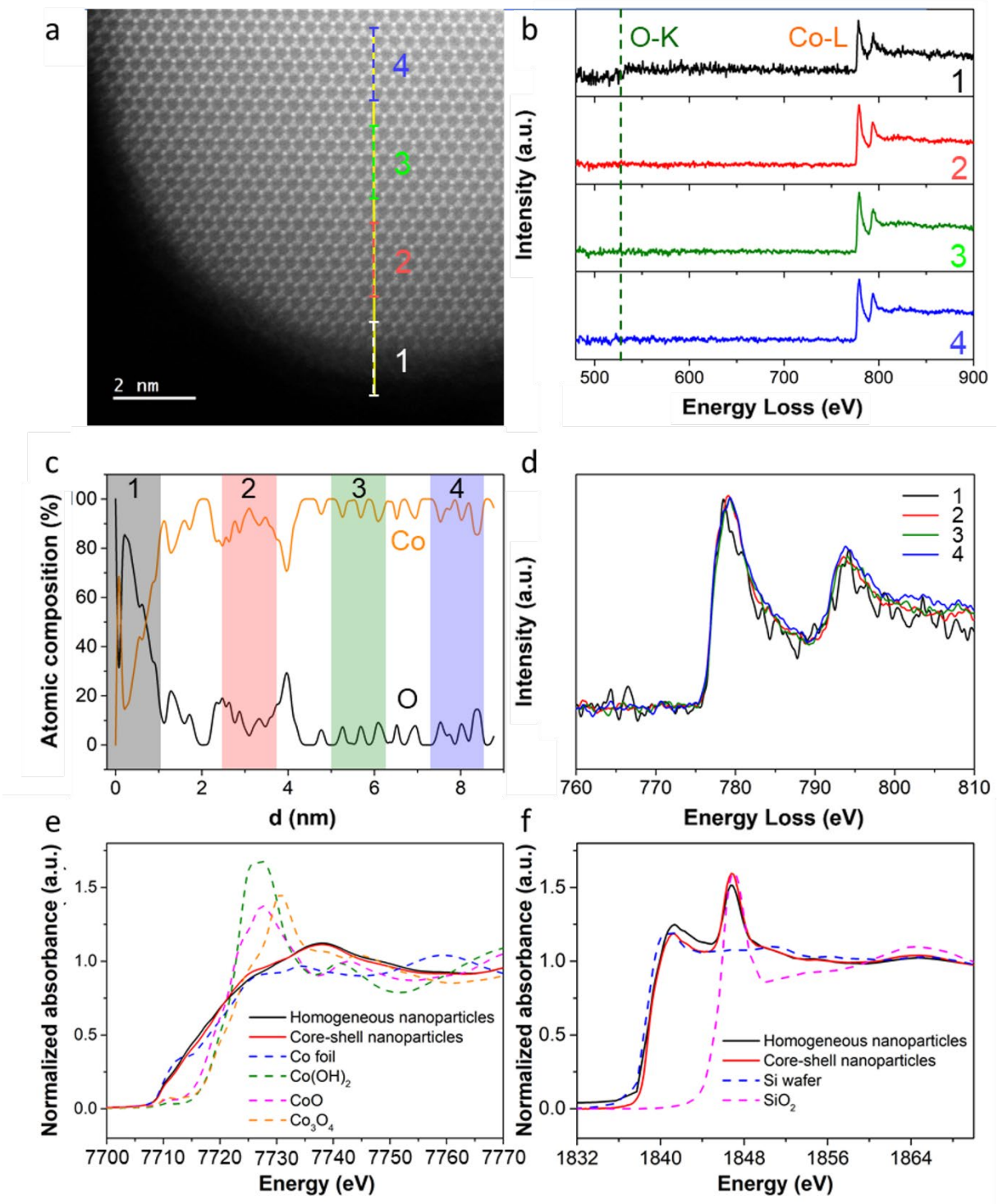

Figure 5. Electronic states in CoSi nanoparticles. (a) Homogeneous CoSi particle STEM-HAADF image, the EELS line scan is shown with the different integration area. (b) EELS spectra, (c) oxygen and cobalt relative contents, (d) Co-L edge and on the different positions marked in a and c. XANES spectra at the (e) Co K- and (f) Si K-edges recorded for homogeneous, core-shell nanoparticles, and for some references.

Unlike bulk CoSi, the nanoparticles obtained in this work respond to a magnet, especially the core-shell nanoparticles. In order to eliminate the possible adventitious influence of ferromagnetic elemental Co clusters not detected by XRD or local TEM analysis, the total X-ray scattering pattern of the core-shell sample was analyzed by pair distribution function (PDF).[35–38] Fitting with only CoSi leads to a fairly acceptable (reliability factor R=20.9%) but yet improvable solution. The addition of crystalline Si and amorphous silica (**Table S2**), in agreement with TEM analysis, yields the best refinement (R=15.6%, **Figure 6**). Amorphous and crystalline Co, as well as amorphous CoO and Co_3O_4, can be excluded since their addition did not improve the reliability factor (**Figure S12**, see experimental methods for details of refinement process). Therefore, the samples are mostly made of CoSi, and do not exhibit elemental cobalt. The magnetic properties of this sample are then attributed to CoSi.

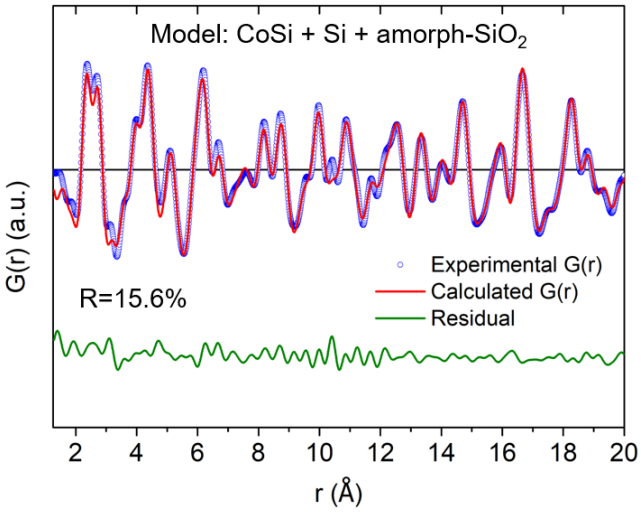

Figure 6. Local structure analysis of core-shell particles. Full X-ray scattering PDF analysis of core-shell CoSi nanoparticles. The calculated *G(r)* has been obtained with a mixture of crystalline CoSi, Si, and amorphous SiO_2.

Enhanced ferromagnetism in cobalt silicide nanostructures

Both core-shell and homogeneous CoSi nanoparticles show ferromagnetic behavior at low temperatures that persist close to room temperature (**Figure 7a-b**). The magnetic properties were evaluated on samples not exposed to air. The core-shell nanoparticles show coercive fields of 15 and 945 Oe at 300 and 5 K, respectively (**Figure 7b**). Similar coercivities were observed for the homogenous sample (**Figure 7a**). The saturated magnetizations (M_s) of both samples were further calculated through the law of approach to saturation.[39,40] For core-shell particles, linear fitting of *M versus* 1/H gives M_s values of 7.9 and 10.6 emu.g^{-1} at 300 K and 5 K, respectively, corresponding to 0.17 and 0.22 μ_B/Co. For homogeneous CoSi particles, the saturated magnetizations of 2.6 (0.048 μ_B/Co) and 3.6 emu g^{-1} (0.067 μ_B/Co) at 300 and 5 K, respectively, are below those of the core-shell particles. These values are much lower than that of metallic Co (1.72 μ_B/Co at 4 K),[8] in agreement with the absence of Co clusters deduced by PDF analysis. Bulk CoSi is reported as intrinsically diamagnetic (**Table S3**).[41] CoSi thin films are also diamagnetic,[6] while single crystal CoSi nanowires showed significant ferromagnetism ascribed to Co atoms in some defective positions, *e.g.* interfaces, grain boundaries and crystal defects.[7,8] Herein, by designing polycrystalline core-shell nanoparticles, we maximize the density of boundaries and interfaces and then interfacial ferromagnetism. This effect is therefore 5-fold and 3-fold more pronounced than for reported CoSi single crystal nanowires (0.03 μ_B/Co at 300 K)[8] and for the homogeneous CoSi nanoparticles prepared in the present work (0.05 μ_B/Co at 300 K), respectively. To evaluate the different contributions to magnetization in the case of the core-shell particles, we analyzed the dependency of *M versus 1/H* up to 9 T at 300 K by following the Honda-Owen approach (**Figure S13**). From these measurements, we observe that about 83 % of the magnetization can be attributed to ferromagnetic species. Some remaining paramagnetic or weakly interacting species may arise from oxo species arising during the washing step.

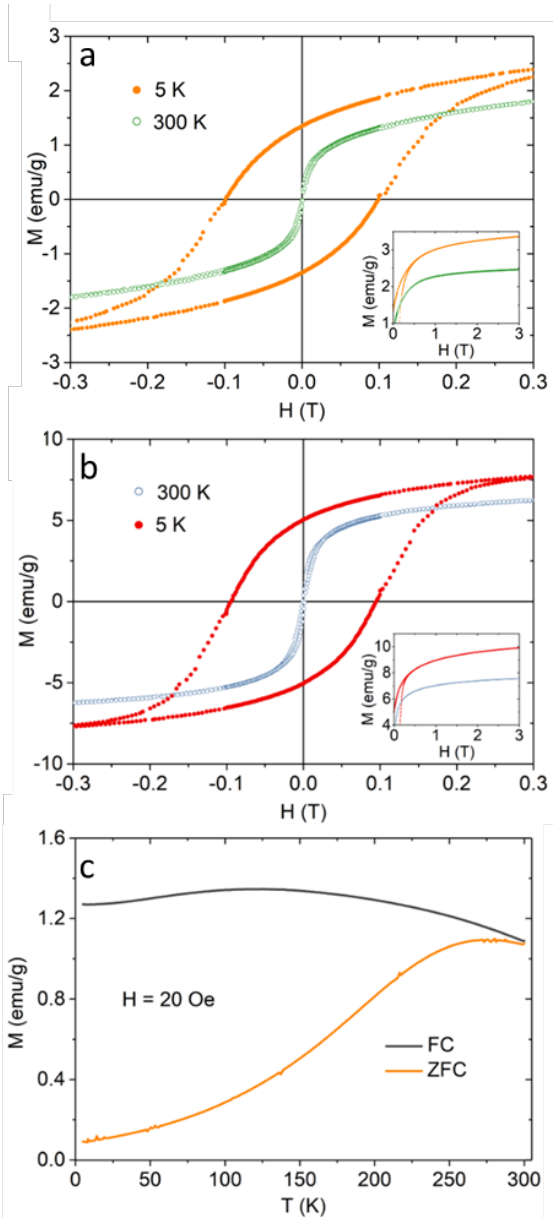

Figure 7. Magnetic properties of homogeneous and of core-shell nanoparticles. (a) Magnetization curves for homogeneous CoSi nanoparticles at 300 and 5 K. (b) Magnetization curves for core-shell nanoparticles (a) *versus* the magnetic field at 300 and 5 K, (b) as a function of temperature at applied field of 20 Oe, recorded after cooling in a 20 Oe field (FC) and after cooling in zero field (ZFC), respectively.

The zero-field cooled (ZFC) magnetization curve of the core-shell nanoparticles (**Figure 7c**) shows a maximum at ca. 275 K. In a polycrystalline CoSi sample, the spins of each crystal domain are spontaneously oriented along their easy axis at room temperature. These macroscopic disordered spin orientations are frozen at low temperature (5 K) before the ZFC

measurement, so that a low magnetization is recorded at the beginning of the ZFC measurement. As the temperature increases, the spins are defrosted to align under the applied field, so the magnetization increases. The rise of temperature also leads to thermal disturbance and decrease of coercivity. As a result, after reaching the maximum magnetization, the field cooled (FC) and ZFC curves converge above 300 K, where the sample no longer shows hysteresis, but an unblocked state with no noticeable hysteresis, which resembles a superparamagnetic state likely influenced by the interparticle dipole-dipole interaction in the powder sample where the particles are not well isolated.

Water oxidation catalysis with cobalt silicide nanostructures

The impact of the homogeneous or core-shell structure of the nanoparticles on the alkaline OER electrocatalytic properties has also been evaluated. A glassy carbon sheet covered with a drop-casted nanoparticles/Nafion film was used as working electrode in a Fe-free 0.1 M KOH electrolyte. The cyclic voltammograms (CVs) of the nanoparticles and of reference commercial IrO_2 nanoparticles are shown in **Figure 8a-b**. Bubbles forming at the surface of the working electrode (not shown) demonstrate the occurrence of OER above 1.5 V vs. the reversible hydrogen electrode (RHE). The two types of silicide nanoparticles show different behaviors in the first CV: the core-shell particles exhibit an irreversible anodic wave at *ca.* 1.2~1.6 V vs. RHE. This wave is not observed in the homogeneous particles. We then assign it to the oxidation of the silicon-rich core of the core-shell particles.[42] After the first cycle, the core-shell particles deliver a steady current density above 1.6 V vs. RHE, with two reversible redox transitions (cathodic waves at *ca.* 1.1 and 1.4 V vs. RHE with constant area along cycling), which could be respectively assigned to the Co(II)/Co(III) and Co(III)/Co(IV) couples.[43,44] These two reversible waves were also observed with the homogeneous nanoparticles, but with

area increasing over cycling until stabilization after *ca.* 13 cycles (**Figure S14**). This suggests that steady-state conditions are reached after these cycles.

After the electrochemical response is stabilized, the overpotential at current density of 10 mA cm^{-2} is 370 and 440 mV for the homogeneous and core-shell nanoparticles, respectively. The activities normalized *versus* the amount of Co were further calculated (**Table S4**). Compared to compounds of cobalt and p-block elements previously studied as OER electrocatalysts (**Table S4** and **Figure S15**), homogeneous and core-shell CoSi nanoparticles show superior normalized OER activity. The anodic potential was then monitored for 15 h at 10 mA cm^{-2} (**Figure 8c**). The increment of potential is negligible over 15 h, testifying a durability for at least 15 h of the properties, and confirming that steady-state conditions are reached.

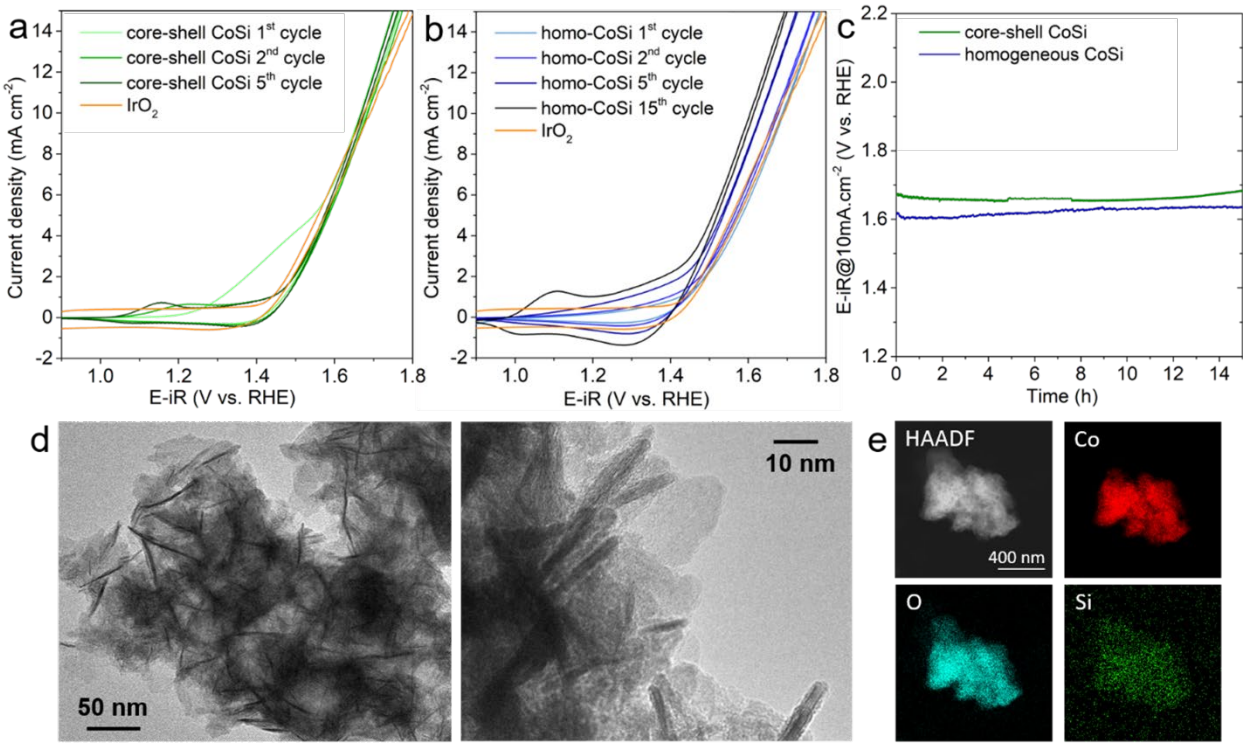

Figure 8. OER electrocatalysis. Selected CVs of (a) core-shell and (b) homogeneous CoSi nanoparticles and of reference commercial IrO_2 nanoparticles in an aqueous O_2-saturated 0.1 M KOH electrolyte. (c) Chronopotentiometry (CP) measurements at 10 mA cm^{-2} for homogeneous and core-shell nanoparticles. (d) TEM images and (e) STEM-EDS chemical mapping of the core-shell nanoparticles after 15 h CP measurement. The elemental maps in (e) are displayed at the same scale as the STEM-HAADF image.

TEM images (**Figure 8d** and **S16**) on post-OER samples show a conversion of the nanoparticles to a layered nanostructure similar for homogeneous and core-shell nanoparticles. STEM-EDS mapping (**Figure 8e**) shows that Co and Si are maintained into the evolved catalyst, with an homogeneous distribution of oxygen. HRTEM (**Figure S17**) shows that the surface of the particles has evolved into a rough layer that contains poorly ordered CoOOH-related nano-objects. EDS and high resolution STEM-EDS (**Figure S18**) further confirm that cobalt, silicon and oxygen are co-located into this layer. XPS analysis (**Figure S19** and corresponding discussion in SI) indicates species consistent with a cobalt oxyhydroxide containing silicon oxoanions.[45] Hence, according to HRTEM, STEM-EDS and XPS, a silicon cobalt oxyhydroxide is the active electrocatalytic species. The silicide nanostructures are then pre-catalysts towards an efficient OER catalyst. According to cyclic voltammetry (**Figure 8a-b**), the conversion to an oxyhydroxide occurs during the first 13 cycles, after which OER stays the only oxidative process above ~1.5 V vs. RHE.

The evolution of the Co and Si oxidation states during OER was further assessed by analyzing the X-ray absorption near edge structure (XANES) of the Si K-edge after OER (**Figure 9a**) and of the Co K-edge (**Figure 9b**) *operando* and after OER. Co and Si K-edge XANES show that the samples are only slightly modified during preparation of the electrodes. Linear combination fittings (LCF) of the Co K-edge XANES of the processed electrodes indicate that only a few percents of the pristine CoSi nanoparticles convert to cobalt(II) oxide (**Figure 9a-c, Tables S5-S6**).[46] *Operando* XAS at the Co K-edge (**Figure S20-21**) was then performed at different potentials with a custom-made cell (**Figure S22**), by starting at the open-circuit voltage (OCV, 0.2 V *vs.* RHE). A down-shift of the Co-K edge energy is observed for both homogeneous and core-shell nanoparticles, which could indicate that the content of oxidized species in the processed electrodes decreases upon immersion, in agreement with LCF

(**Tables S5-S6**). This suggests potential leaching of Co^{2+} species in the electrolyte. Then, 13 CVs (**Figure S23**) were carried out to activate the catalyst as describe above for *ex situ* experiments. Subsequently, chronoamperometry (CA) was performed at 2.0 V vs. RHE for 40 min. The electrode was simultaneously analyzed by XAS. The materials converted progressively to a mixture of CoSi and Co(II)/Co(III)-based oxide/oxyhydroxide, as shown by LCFs of the successive scans (see LCF results in **Tables S5-S6** and the corresponding phase compositions plotted in **Figure S24**), the core-shell particles converting faster than the homogeneous ones, in agreement with *ex situ* experiments. After operation, the electrodes were brought back to the OCV (0.0 V *vs.* RHE). Overall, the materials remained oxidized, suggesting that the conversion of CoSi to cobalt oxide/oxyhydroxide is irreversible. These results are consistent with the *ex situ* XPS and TEM studies. To probe the evolution of silicon, which is difficult to study *by operando* XAS due to the low energy of its K-edge, we analyzed the Si K-edge XANES of an electrode previously subjected to OER for 15 h (**Figure 9c**). The corresponding spectra with a large signal-to-noise ratio indicate that silicon is maintained into the electrode, in agreement with STEM-EDS mapping (**Figure 8e**), which indicates that Co, Si and O are colocalized in the material. The sharp feature at ~1847 eV indicates Si oxoanions (**Figure 5f**). A shoulder at lower energy shows the presence of more reduced Si species, which can be ascribed to silicon bonded to oxygen and to Co, reminiscent of the silicide structure. The Co K-edge EXAFS (**Figure S25**) of the material during OER electrocatalysis (chronoamperometry at 2.0 V vs. RHE) shows predominant peaks corresponding to first Co-O and Co-Co shells with short distances, indicating a Co oxidation state higher than +II, hence a smaller ionic radius,[47] in agreement with XANES and the measured electrochemical behavior. We also observe the emergence of a slight contribution at larger apparent distance, which could be ascribed to a Co-Si distance through CoO_6 octahedra and SiO_4 tetrahedra connected by vertices.[47] Kim *et al.*[47] showed that the incorporation of silicate moieties within amorphous

cobalt phyllosilicates provides structural flexibility to cobalt oxyhydroxide layers. This enables formation of H-bonds that stabilize the OOH* reaction intermediate and reduces the activation energy of its formation, the rate-determining step of OER on cobalt-based catalysts. A similar effect of Si oxoanions derived from the silicide structure may explain the high OER electrocatalytic activity we observe.

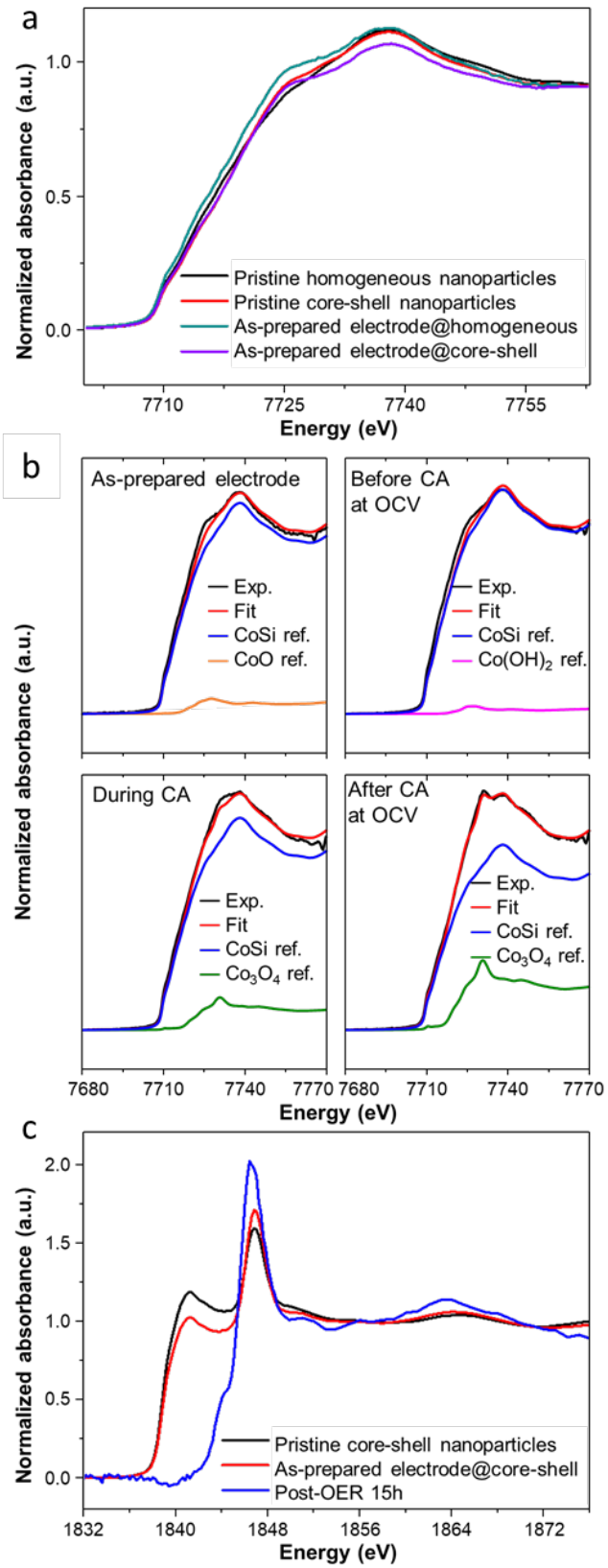

Figure 9. Evolution of cobalt silicide OER electrocatalysts. (a) XANES spectra at the Co K-edge recorded on the homogeneous and core-shell nanoparticles and the corresponding as-prepared electrodes. (b) *Operando* XANES spectra recorded at the Co K-edge during chronoamperometry (CA) and at the open circuit voltage (OCV): Linear combination fits (LCF) of XANES spectra at Co K-edge recorded on threfee electrode prepared with homogeneous

CoSi electrocatalyst at different stages – as prepared electrode before use, and then *operando* at the open circuit voltage (OCV), during chronoamperometry at 2.0 V vs. RHE, and then again at the OCV. The LCF was performed by using as references the XANES spectra of the pristine homogeneous CoSi nanoparticles displayed in (a) and in Figure 5e, as we have demonstrated that Co in this sample is present only as crystalline CoSi. (c) XANES spectra at the Si K-edge showing oxidation of the silicon component after 15 h of OER operation.

CONCLUSIONS

Designing heterostructured nanoparticles of intermetallics with significant covalent character is a challenge due to the high temperatures that these compounds request for structural rearrangement. By using molten salts as high temperature media, we could control the diffusion of cobalt atoms into silicon nanoparticles and then design selectively freestanding homogeneous and core-shell CoSi nanoparticles. The heterostructured particles exhibit increased interface-to-volume ratio and larger density of grain-boundaries in the core-shell nanoparticles. This work shows how controlling the heterostructure of silicon-based intermetallic nano-objects can trigger interface-driven properties, especially strongly enhanced ferromagnetism, with a possible further impact in the science of topological materials.[15] We hypothesize that beyond cobalt silicide, transforming nanocrystals into compounds of metals and p-block elements in molten salts will open the way to new families of heterostructured nanomaterials.

Experimental section

Reagents. Lithium iodide (99%, Alfa Aesar), potassium iodide (99%, Sigma-Aldrich), silicon nanoparticles (99%, Nanomakers©, France) and cobalt(II) chloride (99.7%, Alfa Aesar) were stored and manipulated as received in an Ar-filled glovebox (H_2O < 0.5 ppm, O_2 < 0.5 ppm). Methanol (VWR Normapur grade) was used for washing.

Synthesis of core-shell and homogeneous cobalt monosilicide nanoparticles. 63.2 mg Si nanoparticles (2.3 mmol), 194.8 mg $CoCl_2$ (1.5 mmol), 2.9 g LiI (21.7 mmol) and 2.1 g KI (12.7 mmol) (molar ratio LiI:KI 0.63:0.37) were ball-milled during 2 min at 20 Hz (Retsch MM400 ball mill airtight vial of 50 mL, filled with one steel ball of 62.3 g with a diameter of 23 mm) to get a well-mixed fine powder. The mixture was loaded in a quartz tube (Ø28×H345mm) which was then connected to a Schlenk line and was evacuated under vacuum. An intermediate liquid nitrogen trap between the quartz tube and the Schlenk line was set to condensate the SiI_4 byproduct. A vertical furnace from Eraly® was pre-heated to the reaction temperature 300 and 400 °C for core-shell and homogenous nanoparticles, respectively. Then, the quartz tube was put in the furnace, followed by 6 hours of thermal treatment under dynamic vacuum (10^{-3} mbar). Later, the hot quartz tube was taken out and cooled down to room temperature under vacuum. The as-prepared mixture was washed in methanol by seven cycles of centrifugation/redispersion and was later dried in a Schlenk tube under vacuum during the night. The dried powder was transferred and stored in an Ar-filled glovebox.

Details of characterization methods are provided as supporting information.

ASSOCIATED CONTENT

Supporting Information Available: Experimental details, characterizaztion of the initial Si nanoparticles (Figure S1), additional characterization of the homogeneous CoSi and core-shell nanoparticles (Figures S2-S12, Tables S1-S2), literature survey (Table S3) of magnetic properties and corresponding analyses, electrocatalytic (Table S4, Figure S14) properties of CoSi-related materials, additional data with electrochemical properties (Figure S15) and the characterization of electrocatalysts during OER and post-OER (Figures S16-S24 and Tables S5-S6), additional references.

ACKOWLEDGEMENTS

This project has received funding from the European Research Council (ERC) Consolidator Grant GENESIS under the European Union's Horizon 2020 research and innovation programme (grant agreement n° 864850). Y.S. thanks the China Science Council for funding. The experiments at the SAMBA and LUCIA beamlines at Synchrotron SOLEIL have been funded by SOLEIL as the User Proposal 20210428. J.M. G. C and M. L. R.G acknowledge the support by the Spanish Ministry of Science and Innovation through Research Project PID2020-113753RB-I00. The authors also acknowledge the FCMat platform for TEM and the National Centre for Electron Microscopy (ELECMI National Singular Scientific Facility) for provision of corrected aberration microscopy.

REFERENCES

(1) Schaak, R. E.; Steimle, B. C.; Fenton, J. L. Made-to-Order Heterostructured Nanoparticle Libraries. *Acc Chem Res* **2020**. https://doi.org/10.1021/acs.accounts.0c00520.

(2) Manna, L.; Cheon, J.; Schaak, R. E. Why Do We Care about Studying Transformations in Inorganic Nanocrystals? *Accounts of Chemical Research*. American Chemical Society April 6, 2021, pp 1543–1544. https://doi.org/10.1021/acs.accounts.1c00123.

(3) Reader, A. H.; Van Ommen, A. H.; Weijs, P. J. W.; Wolters, R. A. M.; Oostra, D. J. Transition Metal Silicides in Silicon Technology. *Reports on Progress in Physics* **1993**, *56* (11), 1397–1467. https://doi.org/10.1088/0034-4885/56/11/002.

(4) Nozariasbmarz, A.; Agarwal, A.; Coutant, Z. A.; Hall, M. J.; Liu, J.; Liu, R.; Malhotra, A.; Norouzzadeh, P.; Öztürk, M. C.; Ramesh, V. P.; Sargolzaeiaval, Y.; Suarez, F.; Vashaee, D. Thermoelectric Silicides: A Review. *Jpn J Appl Phys* **2017**, *56*, 0–27. https://doi.org/10.7567/JJAP.56.05DA04.

(5) King, R. B. Topological Aspects of the Chemical Bonding in Superconducting Transition-Metal Borides, Silicides, and Alloys. *Inorg Chem* **1990**, *29* (11), 2164–2170. https://doi.org/10.1021/ic00336a025.

(6) Gomoyunova, M. V.; Grebenyuk, G. S.; Pronin, I. I.; Solov'ev, S. M.; Vilkov, O. Y.; Vyalykh, D. V. Formation and Magnetic Properties of the Silicon-Cobalt Interface. *Physics of the Solid State* **2013**, *55* (2), 437–442. https://doi.org/10.1134/S1063783413020091.

(7) Goldfarb, I.; Cesura, F.; Dascalu, M. Magnetic Binary Silicide Nanostructures. *Advanced Materials* **2018**, *30* (41), 1–11. https://doi.org/10.1002/adma.201800004.

(8) Seo, K.; Varadwaj, K. S. K.; Mohanty, P.; Lee, S.; Jo, Y.; Jung, M. H.; Kim, J.; Kim, B. Magnetic Properties of Single-Crystalline CoSi Nanowires. *Nano Lett* **2007**, *7* (5), 1240–1245. https://doi.org/10.1021/nl070113h.

(9) Liang, S.; Islam, R.; Smith, D. J.; Bennett, P. A.; O'Brien, J. R.; Taylor, B. Magnetic Iron Silicide Nanowires on Si(110). *Appl Phys Lett* **2006**, *88* (11), 113111. https://doi.org/10.1063/1.2185610.

(10) Kumar, R.; Bahri, M.; Song, Y.; Gonell, F.; Thomas, C.; Ersen, O.; Sanchez, C.; Laberty-Robert, C.; Portehault, D. Phase Selective Synthesis of Nickel Silicide Nanocrystals in

Molten Salts for Electrocatalysis of the Oxygen Evolution Reaction. *Nanoscale* **2020**, *12* (28), 15209–15213. https://doi.org/10.1039/d0nr04284f.

(11) Chen, X.; Liang, C. Transition Metal Silicides: Fundamentals, Preparation and Catalytic Applications. *Catal Sci Technol* **2019**, *9* (18), 4785–4820. https://doi.org/10.1039/c9cy00533a.

(12) McEnaney, J. M.; Schaak, R. E. Solution Synthesis of Metal Silicide Nanoparticles. *Inorg Chem* **2015**, *54*, 707–709. https://doi.org/10.1021/ic502394u.

(13) Ryabchuk, P.; Agostini, G.; Pohl, M. M.; Lund, H.; Agapova, A.; Junge, H.; Junge, K.; Beller, M. Intermetallic Nickel Silicide Nanocatalyst—A Non-Noble Metal–Based General Hydrogenation Catalyst. *Sci Adv* **2018**, *4* (6), 1–11. https://doi.org/10.1126/sciadv.aat0761.

(14) Niklas Hausmann, J.; Beltrán-Suito, R.; Mebs, S.; Hlukhyy, V.; Fässler, T. F.; Dau, H.; Driess, M.; Menezes, P. W.; Hausmann, J. N.; Beltrán-Suito, R.; Driess, M.; Menezes, P. W.; Mebs, S.; Dau, H.; Hlukhyy, V.; Fässler, T. F. Evolving Highly Active Oxidic Iron(III) Phase from Corrosion of Intermetallic Iron Silicide to Master Efficient Electrocatalytic Water Oxidation and Selective Oxygenation of 5-Hydroxymethylfurfural. *Advanced Materials* **2021**, *33* (27), 2008823. https://doi.org/10.1002/ADMA.202008823.

(15) Schoop, L. M.; Pielnhofer, F.; Lotsch, B. v. Chemical Principles of Topological Semimetals. *Chemistry of Materials*. American Chemical Society May 22, 2018, pp 3155–3176. https://doi.org/10.1021/acs.chemmater.7b05133.

(16) Sanchez, D. S.; Belopolski, I.; Cochran, T. A.; Xu, X.; Yin, J. X.; Chang, G.; Xie, W.; Manna, K.; Süß, V.; Huang, C. Y.; Alidoust, N.; Multer, D.; Zhang, S. S.; Shumiya, N.; Wang, X.; Wang, G. Q.; Chang, T. R.; Felser, C.; Xu, S. Y.; Jia, S.; Lin, H.; Hasan, M. Z. Topological Chiral Crystals with Helicoid-Arc Quantum States. *Nature* **2019**, *567* (7749), 500–505. https://doi.org/10.1038/s41586-019-1037-2.

(17) Dahal, N.; Chikan, V. Phase-Controlled Synthesis of Iron Silicide (Fe3Si and FeSi2) Nanoparticles in Solution. *Chemistry of Materials* **2010**, *22* (9), 2892–2897. https://doi.org/10.1021/cm100224b.

(18) Kim, J. H.; Kawashima, K.; Wygant, B. R.; Mabayoje, O.; Liu, Y.; Wang, J. H.; Mullins, C. B. Transformation of a Cobalt Carbide (Co3C) Oxygen Evolution Precatalyst. *ACS Appl Energy Mater* **2018**, *1* (10), 5145–5150. https://doi.org/10.1021/acsaem.8b01336.

(19) Chen, P.; Xu, K.; Tong, Y.; Li, X.; Tao, S.; Fang, Z.; Chu, W.; Wu, X.; Wu, C. Cobalt Nitrides as a Class of Metallic Electrocatalysts for the Oxygen Evolution Reaction. *Inorg Chem Front* **2016**, *3* (2), 236–242. https://doi.org/10.1039/c5qi00197h.

(20) Masa, J.; Barwe, S.; Andronescu, C.; Sinev, I.; Ruff, A.; Jayaramulu, K.; Elumeeva, K.; Konkena, B.; Roldan Cuenya, B.; Schuhmann, W. Low Overpotential Water Splitting Using Cobalt-Cobalt Phosphide Nanoparticles Supported on Nickel Foam. *ACS Energy Lett* **2016**, *1* (6), 1192–1198. https://doi.org/10.1021/acsenergylett.6b00532.

(21) Gao, Q.; Huang, C. Q.; Ju, Y. M.; Gao, M. R.; Liu, J. W.; An, D.; Cui, C. H.; Zheng, Y. R.; Li, W. X.; Yu, S. H. Phase-Selective Syntheses of Cobalt Telluride Nanofleeces for Efficient Oxygen Evolution Catalysts. *Angewandte Chemie - International Edition* **2017**, *56* (27), 7769–7773. https://doi.org/10.1002/anie.201701998.

(22) Fan, K.; Zou, H.; Lu, Y.; Chen, H.; Li, F.; Liu, J.; Sun, L.; Tong, L.; Toney, M. F.; Sui, M.; Yu, J. Direct Observation of Structural Evolution of Metal Chalcogenide in Electrocatalytic Water Oxidation. *ACS Nano* **2018**, *12* (12), 12369–12379. https://doi.org/10.1021/acsnano.8b06312.

(23) Masa, J.; Weide, P.; Peeters, D.; Sinev, I.; Xia, W.; Sun, Z.; Somsen, C.; Muhler, M.; Schuhmann, W. Amorphous Cobalt Boride (Co2B) as a Highly Efficient Nonprecious Catalyst for Electrochemical Water Splitting: Oxygen and Hydrogen Evolution. *Adv Energy Mater* **2016**, *6* (6), 1–10. https://doi.org/10.1002/aenm.201502313.

(24) Masa, J.; Schuhmann, W. The Role of Non-Metallic and Metalloid Elements on the Electrocatalytic Activity of Cobalt and Nickel Catalysts for the Oxygen Evolution Reaction. *ChemCatChem*. Wiley Blackwell December 18, 2019, pp 5842–5854. https://doi.org/10.1002/cctc.201901151.

(25) Zhang, M.; Yan, Z.; Li, Y.; Jing, J.; Xie, J. Preparation of Cobalt Silicide on Graphene as Pt Electrocatalyst Supports for Highly Efficient and Stable Methanol Oxidation in Acidic Media. *Electrochim Acta* **2015**, *161*, 48–54. https://doi.org/10.1016/j.electacta.2015.01.221.

(26) Zhang, L.; Chen, X.; Li, C.; Armbrüster, M.; Peng, Z.; Liang, C. Cobalt Silicides Nanoparticles Embedded in N-Doped Carbon as Highly Efficient Catalyst in Selective Hydrogenation of Cinnamaldehyde. *ChemistrySelect* **2018**, *3* (6), 1658–1666. https://doi.org/10.1002/slct.201800007.

(27) Zhang, M.; Pan, D.; Li, Y.; Yan, Z.; Meng, S.; Xie, J. Formation of Cobalt Silicide Nanoparticles on Graphene with a Synergistic Effect and High Stability for Ethanol Oxidation. *RSC Adv* **2016**, *6* (36), 30293–30300. https://doi.org/10.1039/C5RA27496F.

(28) Zhang, L.; Chen, X.; Chen, Y.; Peng, Z.; Liang, C. Acid-Tolerant Intermetallic Cobalt-Nickel Silicides as Noble Metal-like Catalysts for Selective Hydrogenation of Phthalic Anhydride to Phthalide. *Catal Sci Technol* **2019**, *9* (5), 1108–1116. https://doi.org/10.1039/c8cy02258e.

(29) Zhao, A.; Zhang, X.; Chen, X.; Guan, J.; Liang, C. Cobalt Silicide Nanoparticles in Mesoporous Silica as Efficient Naphthalene Hydrogenation Catalysts by Chemical Vapor Deposition. *Journal of Physical Chemistry C* **2010**, *114* (9), 3962–3967. https://doi.org/10.1021/jp9108706.

(30) Ndolomingo, M. J.; Bingwa, N.; Meijboom, R. Review of Supported Metal Nanoparticles: Synthesis Methodologies, Advantages and Application as Catalysts. *J Mater Sci* **2020**, *55* (15), 6195–6241. https://doi.org/10.1007/s10853-020-04415-x.

(31) Portehault, D.; Delacroix, S.; Gouget, G.; Grosjean, R.; Chan-Chang, T. H. C. Beyond the Compositional Threshold of Nanoparticle-Based Materials. *Acc Chem Res* **2018**, *51* (4), 930–939. https://doi.org/10.1021/acs.accounts.7b00429.

(32) Madar, R.; D'Anterroches, C.; Arnaud D'Avitaya, F.; Boursier, D.; Thomas, O.; Senateur, J. P. Magnetic and Transmission Electron Microscopy Studies of the Formation of Cobalt Silicide Thin Films. *J Appl Phys* **1988**, *64* (6), 3014–3017. https://doi.org/10.1063/1.341564.

(33) Zhao, Y.; Feltes, T. E.; Regalbuto, J. R.; Meyer, R. J.; Klie, R. F. In Situ Electron Energy Loss Spectroscopy Study of Metallic Co and Co Oxides. *J Appl Phys* **2010**, *108* (6), 63704. https://doi.org/10.1063/1.3482013.

(34) Sode, J. Spectroscopy and Modelling of Catalyst Nanoparticles Using STEM-EELS, University of Oxford, 2021.

(35) D'Accriscio, F.; Schrader, E.; Sassoye, C.; Selmane, M.; André, R. F.; Lamaison, S.; Wakerley, D.; Fontecave, M.; Mougel, V.; Le Corre, G.; Grützmacher, H.; Sanchez, C.; Carenco, S. A Single Molecular Stoichiometric P-Source for Phase-Selective Synthesis of Crystalline and Amorphous Iron Phosphide Nanocatalysts. *ChemNanoMat* **2020**, *6* (8), 1208–1219. https://doi.org/10.1002/cnma.202000198.

(36) Benseghir, Y.; Lemarchand, A.; Duguet, M.; Mialane, P.; Gomez-Mingot, M.; Roch-Marchal, C.; Pino, T.; Ha-Thi, M. H.; Haouas, M.; Fontecave, M.; Dolbecq, A.; Sassoye, C.; Mellot-Draznieks, C. Co-Immobilization of a Rh Catalyst and a Keggin Polyoxometalate in the UiO-67 Zr-Based Metal-Organic Framework: In Depth Structural Characterization and Photocatalytic Properties for CO2 Reduction. *J Am Chem Soc* **2020**, *142* (20), 9428–9438. https://doi.org/10.1021/jacs.0c02425.

(37) Daoura, O.; Fornasieri, G.; Boutros, M.; El Hassan, N.; Beaunier, P.; Thomas, C.; Selmane, M.; Miche, A.; Sassoye, C.; Ersen, O.; Baaziz, W.; Massiani, P.; Bleuzen, A.; Launay, F. One-Pot Prepared Mesoporous Silica SBA-15-like Monoliths with Embedded Ni Particles as Selective and Stable Catalysts for Methane Dry Reforming. *Appl Catal B* **2021**, *280*, 119417. https://doi.org/10.1016/j.apcatb.2020.119417.

(38) Terban, M. W.; Billinge, S. J. L. Structural Analysis of Molecular Materials Using the Pair Distribution Function. *Chem Rev* **2021**. https://doi.org/10.1021/acs.chemrev.1c00237.

(39) Cullity, B. D.; Graham, C. D. *Introduction to Magnetic Materials*; Wiley, 2011.

(40) Zhang, H.; Zeng, D.; Liu, Z. The Law of Approach to Saturation in Ferromagnets Originating from the Magnetocrystalline Anisotropy. *J Magn Magn Mater* **2010**, *322* (16), 2375–2380. https://doi.org/10.1016/j.jmmm.2010.02.040.

(41) Stishov, S. M.; Petrova, A. E.; Sidorov, V. A.; Krasnorussky, V. N.; Menzel, D. Self-Doping Effects in Cobalt Silicide CoSi: Electrical, Magnetic, Elastic, and Thermodynamic Properties. *Phys Rev B* **2012**, *86* (6), 1–5. https://doi.org/10.1103/PhysRevB.86.064433.

(42) Rakityanskaya, I. L.; Shein, A. B. Anodic Behavior of Iron, Cobalt, and Nickel Silicides in Alkaline Electrolytes. *Russian Journal of Electrochemistry* **2006**, *42* (11), 1208–1212. https://doi.org/10.1134/S1023193506110073.

(43) Smith, R. D. L.; Pasquini, C.; Loos, S.; Chernev, P.; Klingan, K.; Kubella, P.; Mohammadi, M. R.; Gonzalez-Flores, D.; Dau, H. Spectroscopic Identification of Active Sites for the Oxygen Evolution Reaction on Iron-Cobalt Oxides. *Nat Commun* **2017**, *8* (1). https://doi.org/10.1038/s41467-017-01949-8.

(44) Risch, M.; Ringleb, F.; Kohlhoff, M.; Bogdanoff, P.; Chernev, P.; Zaharieva, I.; Dau, H. Water Oxidation by Amorphous Cobalt-Based Oxides: In Situ Tracking of Redox Transitions and Mode of Catalysis. *Energy Environ Sci* **2015**, *8* (2), 661–674. https://doi.org/10.1039/c4ee03004d.

(45) Shen, Y.; Cao, Z.; Wu, Y.; Cheng, Y.; Xue, H.; Zou, Y.; Liu, G.; Yin, D.; Cavallo, L.; Wang, L.; Ming, J. Catalysis of Silica-Based Anode (de-)Lithiation: Compositional Design within a Hollow Structure for Accelerated Conversion Reaction Kinetics. *J Mater Chem A Mater* **2020**, *8* (25), 12306–12313. https://doi.org/10.1039/d0ta01671c.

(46) Saraev, A. A.; Zaikina, O. O.; Sosnin, G. A.; Yeletsky, P. M.; Tsapina, A. M.; Zubavichus, Y. V.; Yakovlev, V. A.; Kaichev, V. V. XAS Study of Mo-Based Dispersed Catalysts for Upgrading of Heavy Oil. *Radiation Physics and Chemistry* **2020**, *175* (March), 1–4. https://doi.org/10.1016/j.radphyschem.2019.05.025.

(47) Kim, J. S.; Park, I.; Jeong, E. S.; Jin, K.; Seong, W. M.; Yoon, G.; Kim, H.; Kim, B.; Nam, K. T.; Kang, K. Amorphous Cobalt Phyllosilicate with Layered Crystalline Motifs as Water Oxidation Catalyst. *Advanced Materials* **2017**, *29* (21). https://doi.org/10.1002/adma.201606893.

Table of Content graphic

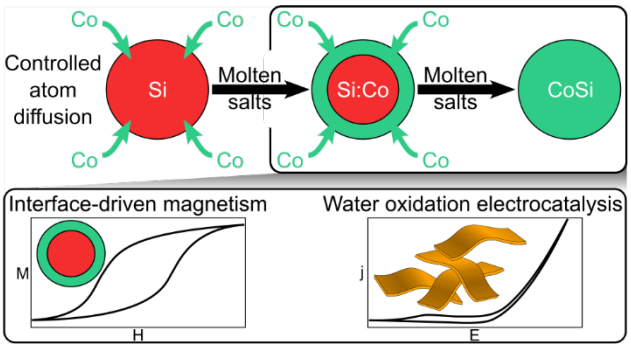

Supporting information

Heterostructured Cobalt Silicide Nanocrystals: Synthesis in Molten Salts, Ferromagnetism, and Electrocatalysis

Yang Song,[a] Isabel Gómez-Recio,[a] Anissa Ghoridi,[a] Fernando Igoa Saldaña,[a] Daniel Janisch,[a] Capucine Sassoye,[a] Vincent Dupuis,[b] David Hrabovsky,[c] M. Luisa Ruiz-González,[d] José M. González-Calbet,[d] Sandra Casale,[e] Andrea Zitolo,[f] Benedikt Lassalle-Kaiser,[f] Christel Laberty-Robert,[a] David Portehault[a,*]

[a] Sorbonne Université, CNRS, Laboratoire de Chimie de la Matière Condensée de Paris (CMCP), 4 place Jussieu, F-75005, Paris, France

[b] Sorbonne Université, CNRS, Laboratoire de Physicochimie des Electrolytes et Nanosystèmes Interfaciaux (PHENIX), 4 place Jussieu, F-75005, Paris, France

[c] Sorbonne Université, CNRS, Institut de Minéralogie de Physique des Matériaux et de Cosmochimie (IMPMC), 4 place Jussieu, F-75005, Paris, France

[d] Dpto. de Química Inorgánica I, Facultad de Ciencias Químicas, Universidad Complutense, 28040 Madrid, Spain

[e] Sorbonne Université, CNRS, Laboratoire de Réactivité de Surface (LRS), 4 place Jussieu, F-75005, Paris, France

[f] Synchrotron SOLEIL, L'Orme des Merisiers, Départementale 128, 91190 Saint-Aubin, France

Corresponding author: david.portehault@sorbonne-universite.fr

Methods

Powder X-ray diffraction (XRD) diagrams were recorded on a Bruker D8 Advance diffractometer operating at the Cu Kα wavelength (λ = 1.5418 Å). CoSi, Co_2Si_3, Co and Si were identified according to the ICDD database and the reference cards 04-012-6522, 04-002-9806, 04-001-2681 and 00-001-0791 respectively.

Energy-dispersive X-ray spectroscopy (EDS) (Oxford Instruments – X-max) was performed on a scanning electron microscope (SEM) HITACHI S3400N at 20 kV. Cobalt was used for calibration of quantitative analyses. Powder samples were flatly smeared on a carbon adhesive tape on sample holder. Spectra were recorded on three to six different zones for each sample.

High-resolution transmission electron microscopy (HRTEM) was carried out on a JEOL JEM 2100Plus FEG microscope (Tokyo, Japan) operating at 200 kV with a spatial punctual resolution of 1.8 Å equipped with X-ray Energy Dispersive Spectroscopy (EDS) for chemical analysis and JEOL-JEM Grand ARM 300cF microscope (Madrid, Spain) equipped with a Cs Corrector (ETA-JEOL) and CMOS camera (4096 x 4096 pixels, Gatan OneView) at 80 kV. **Transmission electron microscopy** (TEM) images were acquired on a Tecnai Spirit 2 microscope operating at 120 kV. The samples were prepared by depositing a drop of ethanolic suspension on carbon coated Cu grids.

Scanning transmission electron microscopy (STEM) and Energy Electron Loss Spectroscopy (EELS) study was performed in JEOL JSM-ARM200F (Cold Emission Gun), probe spherical aberration corrected microscope operating at 120 kV. High angle-annular dark field (HAADF) images were recorded at 68-280 mrad inner and outer collection semi-angles. EELS study was performed by using a GIF-QuantumER with a collection convergence semiangle of 18 mrad and 20.3 mrad, respectively. EELS spectra were acquired by using spectrum line and 2D mode, with 0.25 eV dispersion and 0.05 s acquisition time and an over an average of 100 points per particle. Principal component analysis (PCA) was performed on EELS data to improve signal to noise ratio by using the multivariate statistical analysis (MSA) plugins for GatanDMS software.[1]

Cobalt and silicon oxidation state have been qualitatively evaluated. In the case of silicon, the Si K-edge shape drastically changes depending on the oxidation state, metallic silicon and silica (SiO_2) have been used as standards. On the other hand, the cobalt oxidation state has been studied by considering Co-$L_{2,3}$ edge shape. Traditionally, in oxides the $L_{2,3}$ ratio and cobalt oxidation state relationship is described by a monotonic dependence. However, this approach is not valid on non-oxides materials, since metallic cobalt presents an intermediate $L_{2,3}$ value between Co^{2+} and Co^{3+}. As a consequence using the $L_{2,3}$ ratio is not suitable to study silicon intermetallics. Previous works have described the use of the Co- $L_{2,3}$ edge shape as oxidation state indicator. [2–4]

Pair Distribution Function (PDF) X-ray scattering data were acquired on a Bruker D8 advance diffractometer equipped with a Göbel mirror and a LYNXEYE detector, with Mo Kα radiation (mean λ(Kα1α2) = 0.71073 Å) at room temperature. The powder sample was loaded in a Ø 0.5 mm borosilicate capillary. Measurements were performed from Q_{min} = 0.12 $Å^{-1}$ to Q_{max} = 17.0 $Å^{-1}$ (($Q = \frac{4\pi\sin\theta}{\lambda}$) on rotating capillaries with evolving counting parameters as a function of the *Q*-range in order to optimize the counting rate at high *Q*. The final powder XRD diagram was thus obtained from the combination of 7 patterns ($2\theta_i$ (°)- $2\theta_f$ (°)- step size (°)- step time (°): 0.8-31-0.02-2, 29-61-0.04-6, 59-91-0.06-15, 89-121-0.1-40 twice, 119-150-0.1-100 twice) for a total measuring time of 34 h. Additional scattering measurements from the empty capillary were performed in the same conditions for background subtraction. Raw data were treated using the PDFgetX3 program[5] to obtain the total *G*(*r*) function, using the following parameters: Q_{min} = 0.15 $Å^{-1}$, Q_{max} = 16.6 $Å^{-1}$, r_{poly} = 1.75.

PDF refinements. All refinement were performed for the core-shell CoSi nanoparticles using PDFGui[6] in the range 1.3-20 Å. The best local structure description is obtained when the calculated $G(r)_{calc}$ from the refined structure is the closest to the experimental $G(r)_{exp}$, where the reliability *R* factor is at its lowest (**Table S3**). CoSi with 9 nm coherence length was used as a starting point. Cell parameters, scale

factor, thermal parameters, atomic positions and peak broadening effect (*sratio* and *rcut*) parameters were allowed to vary, and led to an acceptable but perfectible reliability factor of 20.9%.

Additional phases where then added, taking into account results from the core-shell CoSi XRD pattern: presence of crystalline Si in small amounts and strict absence of any crystalline impurities such as CoO, Co_3O_4, Co_2Si_3, KI or SiI_4. The addition of these compounds was thus tested during PDF refinements as amorphous phases. Crystalline cobalt appeared highly unlikely according to XRD, although it could not be totally excluded given the proximity and width of CoSi intense peaks. Therefore, we used PDF analysis to assess the presence of crystalline or amorphous cobalt.

Crystalline Si and/or amorphous SiO_2 (coherence length 8Å) were then added in the structural model, by firstly adapting the fixed scale factor ratio between 0 and 1 with a step of 0.1 (only the optimal ratios are presented in **Table S3**), then allowing the scale factors to be refined. The reliability factor *R* for CoSi/amorphous SiO_2/crystalline Si mixture decreased down to 15.6%, better than CoSi alone, CoSi/amorphous SiO_2 (*R* =20.1%) or CoSi/crystalline Si mixture (*R* = 19.7%). This is the decrease of the reliability factor that allows us to validate the addition of a new phase in the mixture.

Crystalline cobalt was also tested as additional phase (in addition to CoSi, amorphous SiO_2 and crystalline Si) with PDF analysis. The refinement got worse with this phase addition (*R* = 15.9% when the Co amount was fixed, and negative scale factors when it was allowed to vary), meaning that the presence of crystalline Co is highly improbable.

Amorphous Co was also tested in addition to the CoSi / amorphous SiO_2 / crystalline Si mixture. It did not improve the refinement (*R* = 15.8% when fixed, negative scale factors when allowed to vary). A CoSi and amorphous Co mixture was tested as well and compared with CoSi alone. This led to a slightly worse reliability factor (21.0%) than CoSi alone. The degradation of CoSi-alone refinement resulting from adding amorphous Co and the lack of improvement of the refined CoSi / amorphous SiO_2 / crystalline Si mixture allow us to eliminate amorphous Co as a component of the material.

Similarly, the addition of amorphous CoO, Co_3O_4, KI, SiI_4 or Co_2Si_3 did not improve the refinement (increase of the reliability factors and/or negative scale factors when allowed to vary), thus excluding their presence.

The lowest reliability factor has thus allowed us to validate the CoSi / amorphous SiO_2 / crystalline Si mixture. In absence of a strong structural relationship (epitaxy) between the phases, the refined scale factors are roughly proportional to the squared number of contributing electrons of each phase within the scattering volume, or more roughly to its atomic number density weighted percent, which is generally close to its mass percent.[7] The mixture can thus be semi-quantified as the 64 wt. % CoSi / 26 wt. % amorphous SiO_2 / 10 wt. % crystalline Si mixture.

X-ray photoelectron spectroscopy (XPS) analyses were performed on an Omicron Argus X-ray photoelectron spectrometer, equipped with a monochromated AlKα radiation source (1486.6 eV) and a 280 W electron beam power. Binding energies were calibrated against the C 1s (C-C) binding energy at 284.8 eV. Raw data were treated on Thermo Scientific™ Avantage.

Magnetic measurements. Vibrating sample magnetometry (VSM) on quantum design PPMS was used to determine the curves of magnetization versus applied field at 5 and 300 K for the samples. Zero-field-cooled and field-cooled magnetization versus temperature curves were acquired on a Quantum Design MPMS-XL superconducting quantum interference device (SQUID) magnetometer at magnetic field of 20 Oe from 5 K to 300 K. All measurements were performed on powder samples.

Electrochemical measurements. A typical three-electrode configuration was used, which includes a working electrode, a Pt coil as counter electrode and an Ag/AgCl saturated KCl electrode as reference electrode. Glassy carbon sheets were used for the working electrode. The working electrode was prepared by drop casting. 3.4 mg of catalyst was sonicated in 480 µL absolute ethanol for 15 min, followed by adding 20 µL of Nafion solution (5% in alcohols and water, Sigma-Aldrich) for another 10 min of ultrasonication. The well-dispersed ink was then dropped onto the GC sheet substrate to obtain

a catalyst loading of 170 $\mu g_{catalyst}$ $cm^{-2}_{electrode}$, and then the substrate was dried for at least 30 min under air.

The electrolyte was bubbled with O_2 for at least 20 min before measurement. Cyclic voltammograms (CV) were recorded from 0 to 1.05 V vs. saturated KCl Ag/AgCl reference electrode at scan rate of 20 mV s^{-1}, until overlapped cycles were obtained. For the chronopotentiometry (CP), the current density was set at 10 mA cm^{-2} to monitor the potential evolution.

The ohmic drop iR compensation was performed for the potentials reported, where the resistance is approximately equal to the total impedance measured at a frequency of 50 kHz. The potentials vs. the reversible hydrogen electrode (RHE) were obtained from conversion of measured potentials based on the equation: $E_{RHE} = E_{measured} + 0.197 + 0.0591\times$ pH.

***Ex situ* XAS experiments.** XAS analysis were performed at synchrotron SOLEIL, on the LUCIA beamline for the Si-K edge and on the SAMBA beamline for the Co-K edge, with a ring current of 500 mA and a nominal energy of 2.3 GeV. At LUCIA, the incident beam energy was monochromatized using a Si 111 double crystal monochromator. Data were collected in a primary vacuum chamber as fluorescence spectra with an outgoing angle of 5 ° using a Bruker silicon drift detector. The data were normalized by the intensity of incident energy and processed with the Athena software. Powder samples were measured as pellets prepared by pressing mixtures of nanoparticles and boron nitride powders. Electrode samples were measured as prepared and as recovered for electrochemical measurement. For the Co-K edge, the SAMBA beamline is equipped with a sagittally focusing Si 220 monochromator and two Pd-coated mirrors that were used to remove X-rays harmonics. The powders were pelletized as disks of 10 mm diameter with 1 mm thickness using 2 mg sample powder and 40 mg cellulose powder as a binder.

***Operando* XAS experiments.** *operando* XAS at the Co-K edge was performed at the SAMBA beamline of SOLEIL. The spectra were acquired by recording the K_α X-ray fluorescence of Co with a Canberra 35-elements monolithic planar Ge pixel array detector. The electrochemical methods were the same as described above, except that the working electrode was installed in a different custom-made electrochemical cell of three-electrode configuration where one of the faces of the working electrode is exposed for X-ray analysis (**Figure S22**). Four electrochemical stages were programmed, including successively a first OCV for 20 min, 13 cycles of CV from 1.0 to 2.0 V vs. RHE, chronoamperometry (CA) at 2.0 V vs. RHE for 40 min, and a second OCV for 20 min. The ohmic drop iR correction was not carried out in these measurements. Meanwhile, the XAS spectra were acquired at four different states of the electrode and five scans were repeated for each state (acquisition time of 4 min for each spectrum). Firstly, the installed dry electrode was measured before adding electrolyte in the cell. Then, the electrode in contact with electrolyte was measured during the first OCV. A third measurement was performed during CA. Finally, the XANES was measured when the electrode was brought back to the OCV.

Linear combination fitting (LCF) for XANES. XAS data processing were carried out with the Athena software. Normalized $\mu(E)$ spectra were fitted in the range from -20 to 60 eV (vs. E_0). The references of CoO, $Co(OH)_2$ and Co_3O_4 were provided by the beamline laboratory. The CoSi reference used for fitting was produced by the synthesis reported in this work.

Characterization

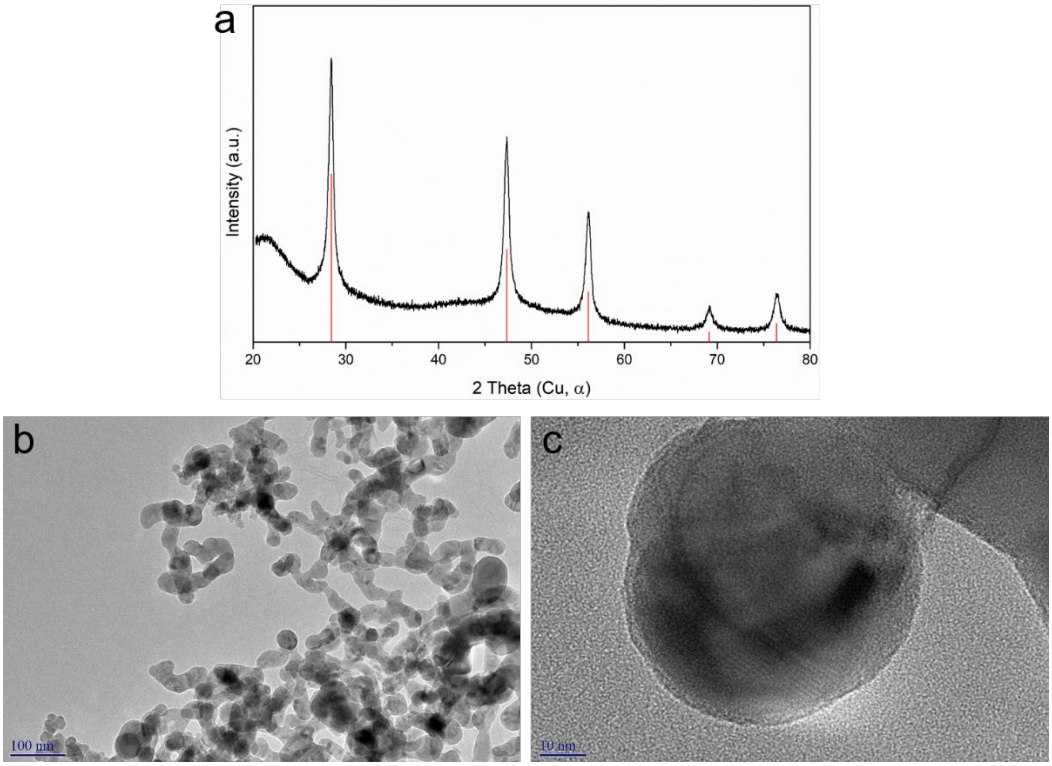

Figure S1. (a) Powder XRD pattern of Si nanoparticles used as reagents. Red drop lines indicate the diamond-like structure Si reference. (b-c) TEM images of Si nanoparticles used as reagents.

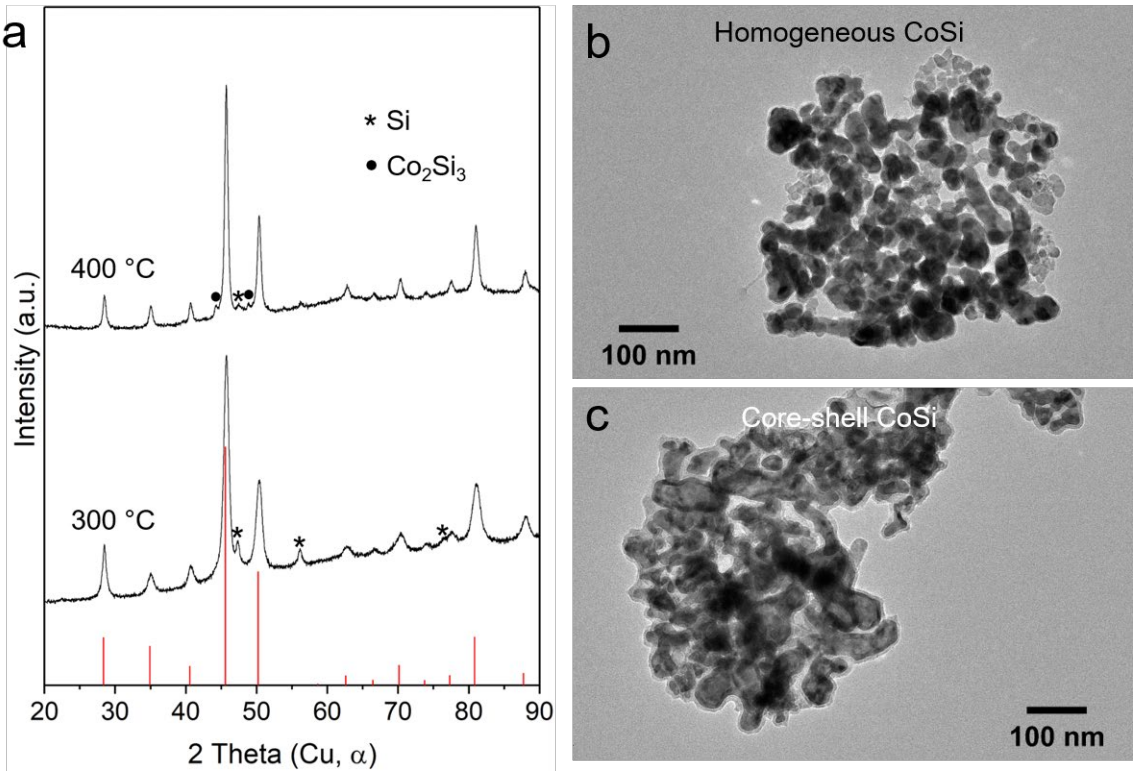

Figure S2. Comparison of (a) powder XRD diagrams of CoSi samples obtained at 400 and 300 °C. TEM images of corresponding (b) homogeneous CoSi and (c) core-shell nanoparticles.

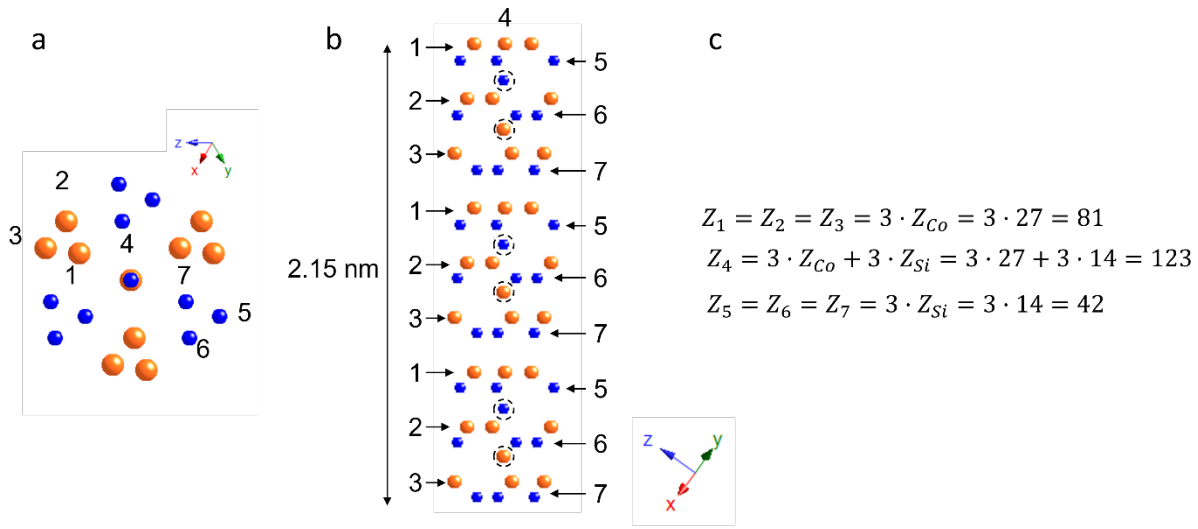

Figure S3. Schematic drawing of the CoSi structure along (a) the $[1\bar{1}\bar{1}]$ direction and (b) the $[110]$ direction perpendicular to $[1\bar{1}\bar{1}]$. (c) Cumulative atomic number of b atomic columns in a 2.15 nm-thick crystal.

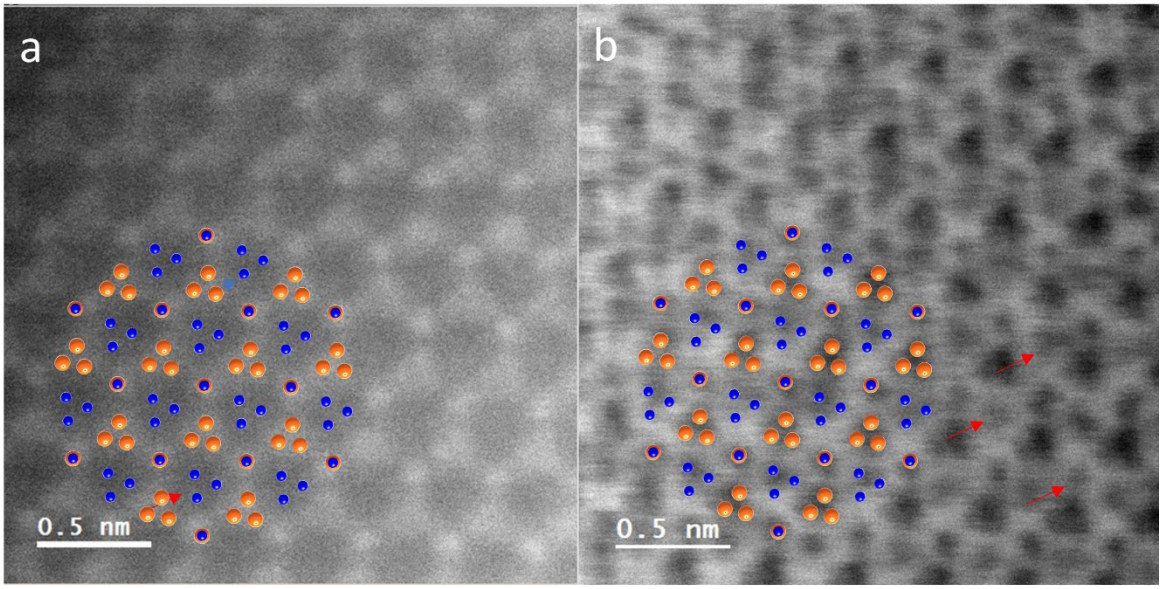

Figure S4. (a) STEM-HAADF and (b) STEM-ABF images of a homogeneous CoSi particle oriented along $[1\bar{1}\bar{1}]$ zone axis. STEM-HAADF provides brighter contrast for heavy elements (Co), while STEM-ABF provides brighter contrast for light elements (Si).

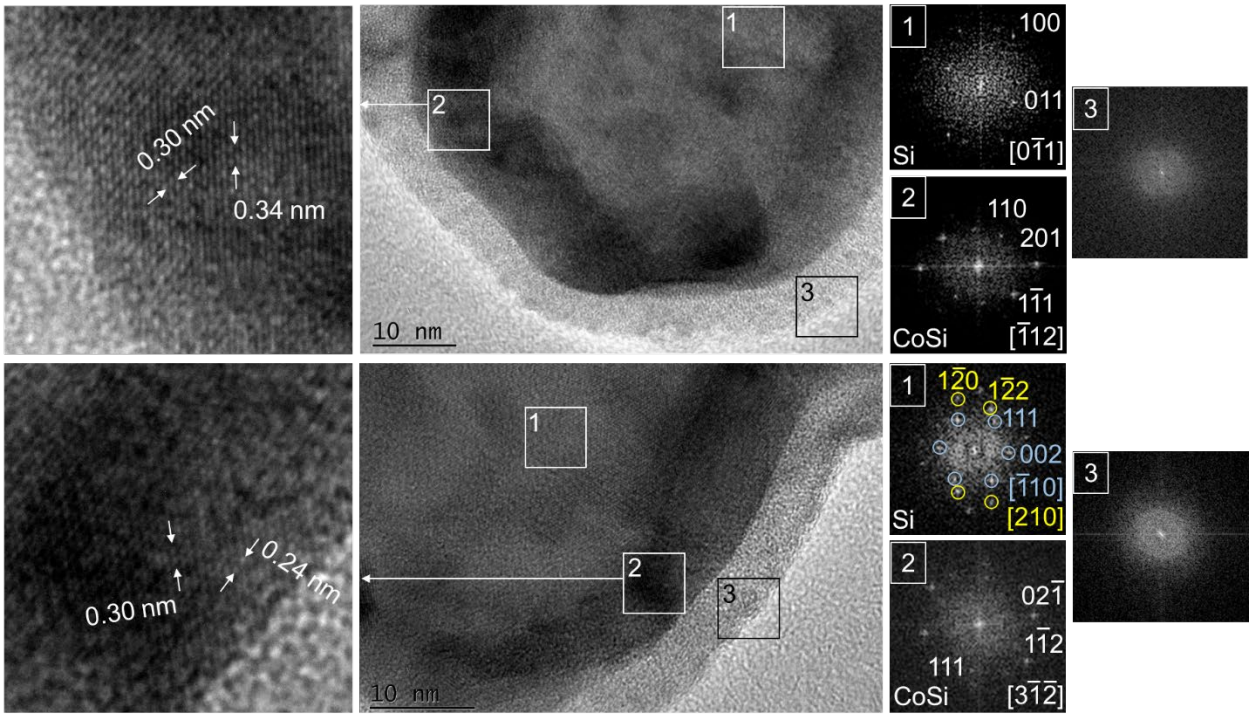

Figure S5. HRTEM images of core-shell CoSi nanoparticles and the FFTs of corresponding areas. Crystal domains in the core and the shell are indexed along d-Si and CoSi structures, respectively. The lighter contrast outer layer shows no crystalline feature and is ascribed to surface oxidation.

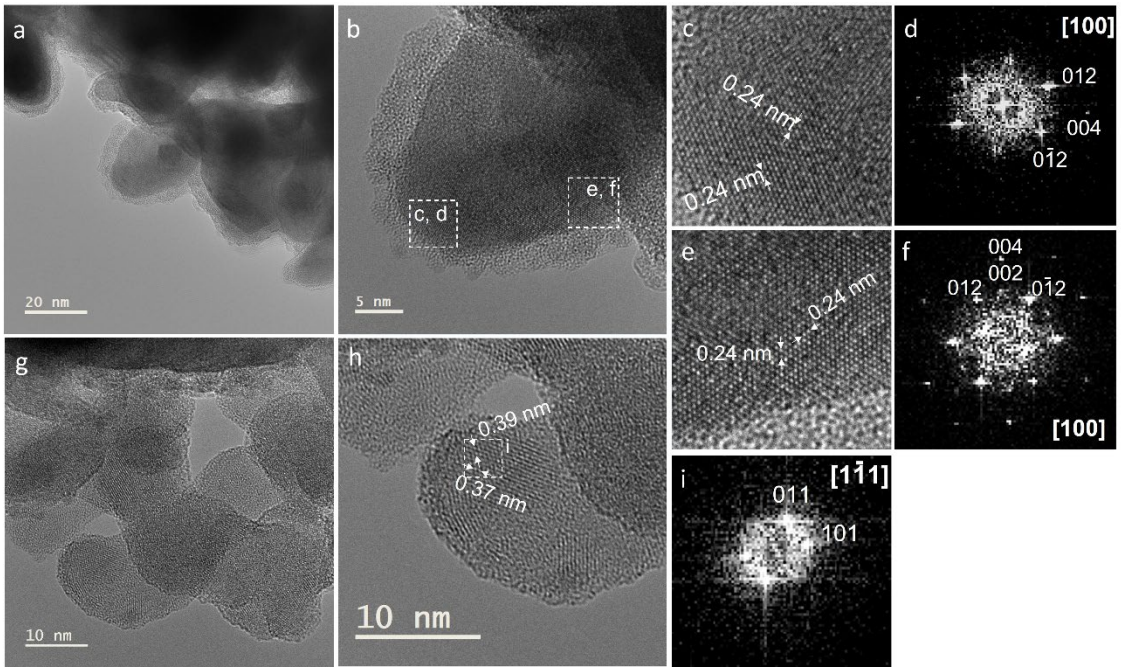

Figure S6. Small homogeneous CoSi nanoparticles detected at 300 °C: (a, g) TEM, (b, c, e, h) HRTEM images and (d, f, i) corresponding FFTs indexed along the CoSi structure. The amorphous layer in (a) is consistent with a silica passivation layer, as discussed in the main text in relation with TEM, STEM-ABF (Figures S5 and 4c), STEM-HAADF (Figure 3a) and STEM-EELS (Figure S7c-d and S8c-d).

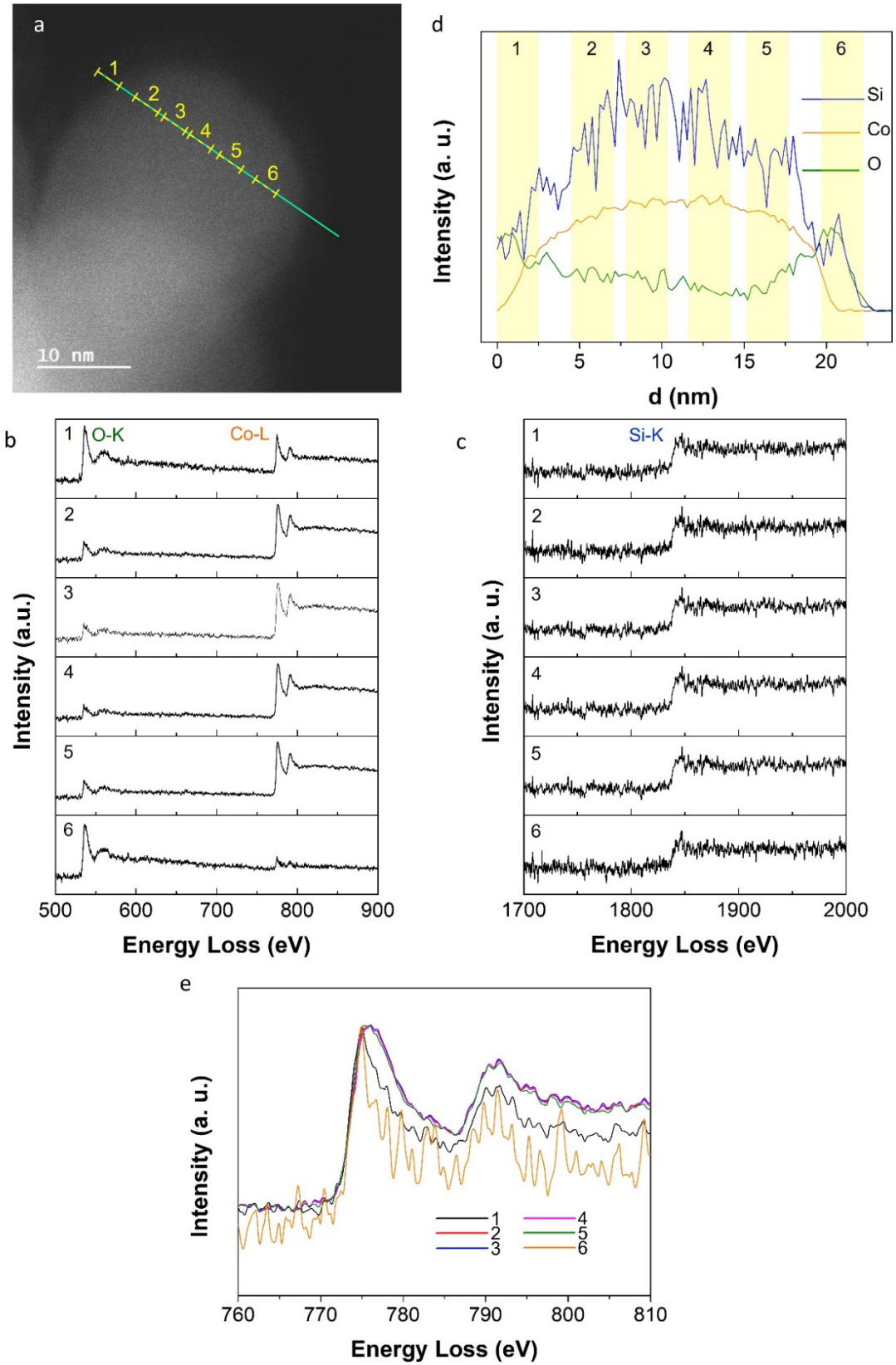

Figure S7. (a) STEM-HAADF image of a homogeneous CoSi nanoparticle obtained at 300 °C, showing the STEM-EELS linear scan. (b) O-K, Co-L and (c) Si-K edge regions of the EELS spectra at the different positions of the linear scan. (d) Si, Co and O EELS intensity profiles. (e) Normalized intensity Co-K EELS spectra at the different regions.

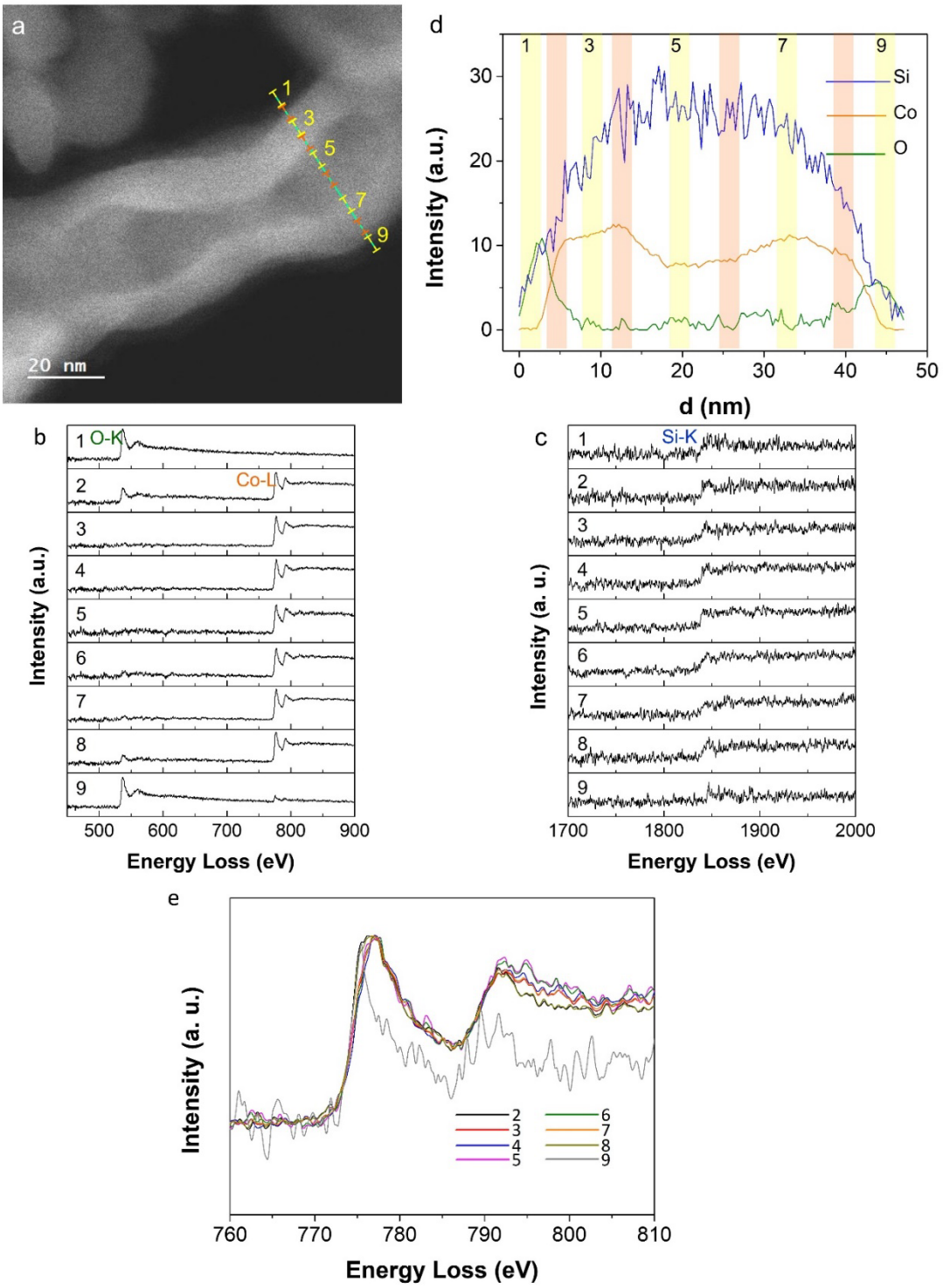

Figure S8. (a) STEM-HAADF image of a core-shell nanoparticle obtained at 300 °C, showing the STEM-EELS linear scan. (b,) O-K, Co-L and (c) Si-K edge regions of the EELS spectra at the different positions of the linear scan. (d) Si, Co and O EELS intensity profiles. (e) Normalized intensity Co-K EELS spectra of the different regions.

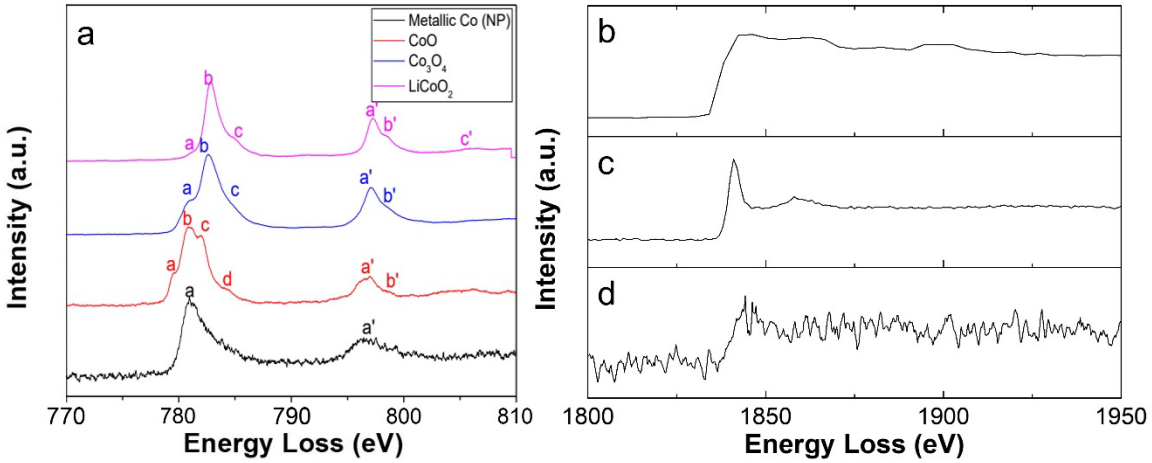

Figure S9. (a) EELS Co-$L_{2,3}$ edge of metallic Co nanoparticles, CoO, Co_3O_4 and $LiCoO_2$ standards. EELS Si-K edge of (b) Si standard, (c) SiO_2 standard and (d) CoSi samples synthesized in this work. (a) is adapted from a work of J. Sode[2]. The EELS data for Si and SiO_2 are provided from the core-loss Atlas library implemented in the Gatan Microscopy Suite 3 software.[8]

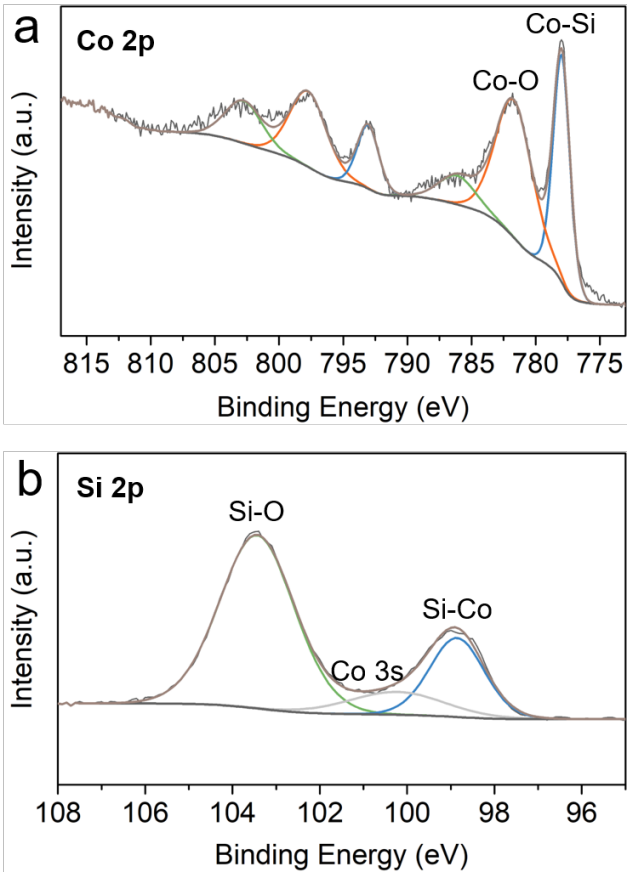

Figure S10. XPS of as-prepared core-shell nanoparticles: (a) Co 2p and (b) Si 2p regions. The peak at 100.2 eV is due to the photoelectron emission from the Co 3s state.[9] The Co $2p_{3/2}$ region shows peaks at 778.0 eV and 781.7 eV, which can be ascribed to the cobalt silicide and to oxidized cobalt formed by air exposure, respectively.[10–12] In the Si region, a peak at 103.4 eV corresponds to silicates and SiO_2. The component at 98.6 eV can be assigned to metal silicides.[13–15]

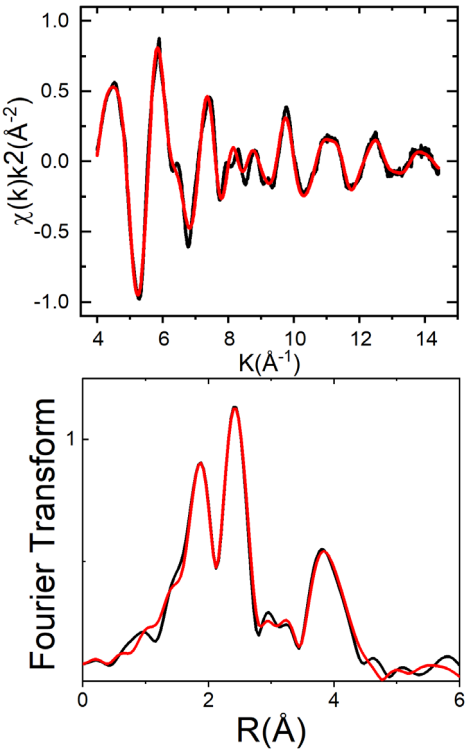

Figure S11. Co K-edge EXAFS analysis of homogeneous CoSi nanoparticles. Upper panel: the theoretical signal (red line) superimposed to the experimental one (black line). Lower panel: the fit in the Fourier transformed space, without phase-shift correction applied. **Table S1** sums up the structural parameters obtained from the fitting procedure.

The EXAFS analysis was performed with the GNXAS code.[16,17] In the GNXAS approach the interpretation of the experimental spectrum is based on the decomposition of the EXAFS χ(k) signal into a summation over *n*-body distribution functions $\gamma^{(n)}$ calculated by means of the multiple-scattering (MS) theory. Each signal has been calculated in the Muffin-tin (MT) approximation using the Hedin-Lundqvist (HL) energy dependent exchange and correlation potential model, which includes inelastic loss effects. Least-square fits of the EXAFS raw experimental data have been performed by minimizing a residual function of the type:

$$R_i\left(\{\lambda\}\right) = \sum_{i=1}^{N} \frac{[\alpha_{\exp(E_i)} - \alpha_{mod}(E_i\,;\,\lambda_1, \lambda_2, \ldots, \lambda_p)]^2}{\sigma_i^2}$$

where N is the number of experimental points, *Ei* = (λ_1, λ_2,..., λ_p) are the p parameters to be refined and σ_i^2 is the variance associated with each experimental point $\alpha_{exp(Ei)}$. Additional non-structural parameters were minimized, namely E_0 (core ionization threshold energy) and S_0^2 (amplitude reduction factor) which considers intrinsic losses. The fit was carried out using the crystallographic structure of CoSi as reported in the main text, then fixing the coordination numbers to crystallographic ones, and only allowing the Co-Si and Co-Co distances to vary. The agreement between the experimental and theoretical spectra is very good, and the bond metrics derived from the fitting procedure are in excellent agreement with the reported crystallographic data from the ICSD database.

Table S1. Best-fit parameters obtained from the analysis of the EXAFS spectrum of CoSi. *CN* is the coordination number, *R* is the interatomic distance, σ^2 is the Debye-Waller factor. Errors are given in brackets (for example 2.33(1) means 2.32-2.34).

	***CN* (fixed)**	***R* (Å)**	**σ^2 (10^{-3} Å^2)**
Co-Si1	4	2.33(1)	3.9(5)
Co-Si2	3	2.41(3)	4.3(7)
Co-Co1	6	2.71(2)	1.1(2)
Co-Si3	3	3.62(1)	15(5)
Co-Co2	3	3.97(4)	6.7(1.5)
Co-Si4	3	4.17(1)	2.3(1.0)
Co-Si5	3	4.22(1)	5.3(9)
Co-Co3	6	4.37(1)	9.8(2)
Co-Co4	6	4.43(2)	6.6(1.0)
Co-Si6	3	4.65(3)	9.0(2)
Co-Co5	6	5.18(2)	10(5)
Co-Co6	6	5.95(2)	4.7(3)
Co-Co7	12	6.29(5)	2.3(3)

Table S2. Successive refinements that have led to the optimum CoSi / am SiO_2/ cryst Si model. *f* stands for "fixed parameters" and *v* for "variable parameter".

Phases refined	Scale factors	Rw (%)
CoSi	1	20.9
CoSi / cryst Si	f: 0.9 / 0.1	19.7
CoSi / cryst Si	0.90 / 0.10 *v: x / 1-x*	19.7
CoSi / am SiO_2	f: 0.8 / 0.2	20.2
CoSi / am SiO_2	0.75 / 0.25 *v: x / 1-x*	20.1
CoSi / am SiO_2 / cryst Si	f: 0.7 / 0.2 / 0.1	15.8
CoSi / am SiO_2 / cryst Si	**0.64 / 0.26 / 0.10** ***v: x / y / 1-x-y***	**15.6**
CoSi / am SiO_2 / cryst Si / cryst Co	f: 0.6 / 0.2 / 0.1 / 0.1	15.9
CoSi / am SiO_2 / cryst Si / cryst Co	CoSi over 1 *v: x / y / z / 1-x-y-z*	
CoSi / am SiO_2 / cryst Si / cryst Co	0.63 / 0.26 / 0.10 / 0.01 *v: 0.64x / 0.26x / 0.10x / 1-x*	15.7
CoSi / am SiO_2 / cryst Si / am Co	f: 0.6 / 0.2 / 0.1 / 0.1	15.8
CoSi / am SiO_2 / cryst Si / am Co	CoSi over 1 *v: x / y / z / 1-x-y-z*	
CoSi / am SiO_2 / cryst Si / am Co	0.63 / 0.25 / 0.10 / 0.02 *v: 0.64x / 0.26x / 0.10x / 1-x*	15.7

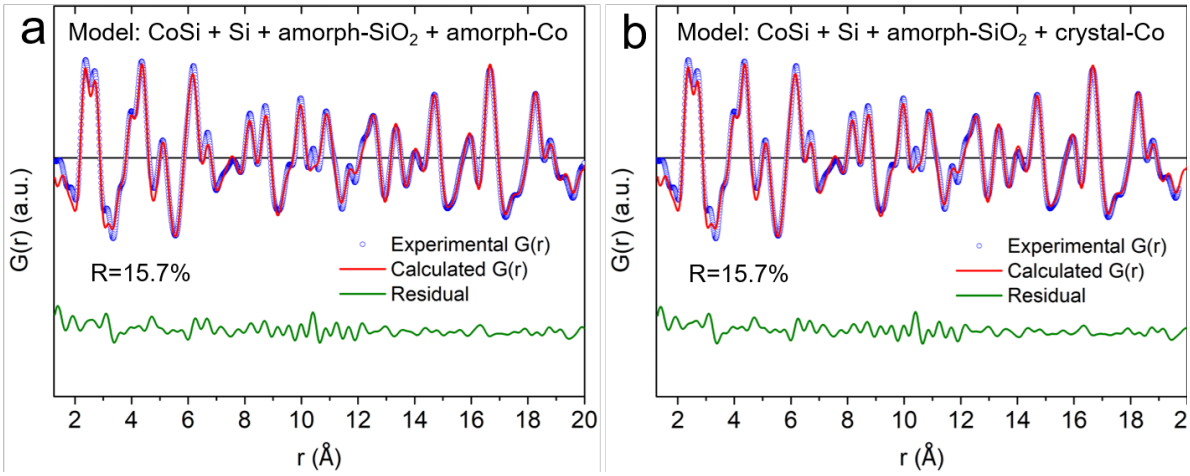

Figure S12. The experimental data (blue dotted line) of core-shell nanoparticles superimposed with the calculated PDFs (red line) of different models, and residual profiles (green).

Table S3. Comparison of the magnetic properties of different Co-based materials.

Phase	Morphology	Temperature (K)	Coercivity (Oe)	Saturation magnetization		Ref.
				μ_B/Co	emu g^{-1}	
CoSi	Polycrystalline core-shell nanoparticles	300	15	0.17	7.7	This work
		5	945	0.22	10.6	This work
CoSi	Polycrystalline nanoparticles (40 nm)	300	5	0.05	2.6	This work
		5	1000	0.07	3.6	This work
CoSi	Single crystal nanowires (20-60 nm)	300	460	0.03	1	18
CoSi	Thin film	-	non-magnetic			19
CoSi	Bulk	<20	diamagnetic			20
Co_3B	Nanoparticles (10-20 nm)	300	1300	-	-	21
		5	1400	1.02	91	21
Co	Nanoparticles (1.5 nm)	5	-	1.94	185	22
Co	Nanoparticles (1.5 nm) surface covered by CO	5	-	0.58	55	22
Co	Thin film	4.2	1000	1.72	166	23

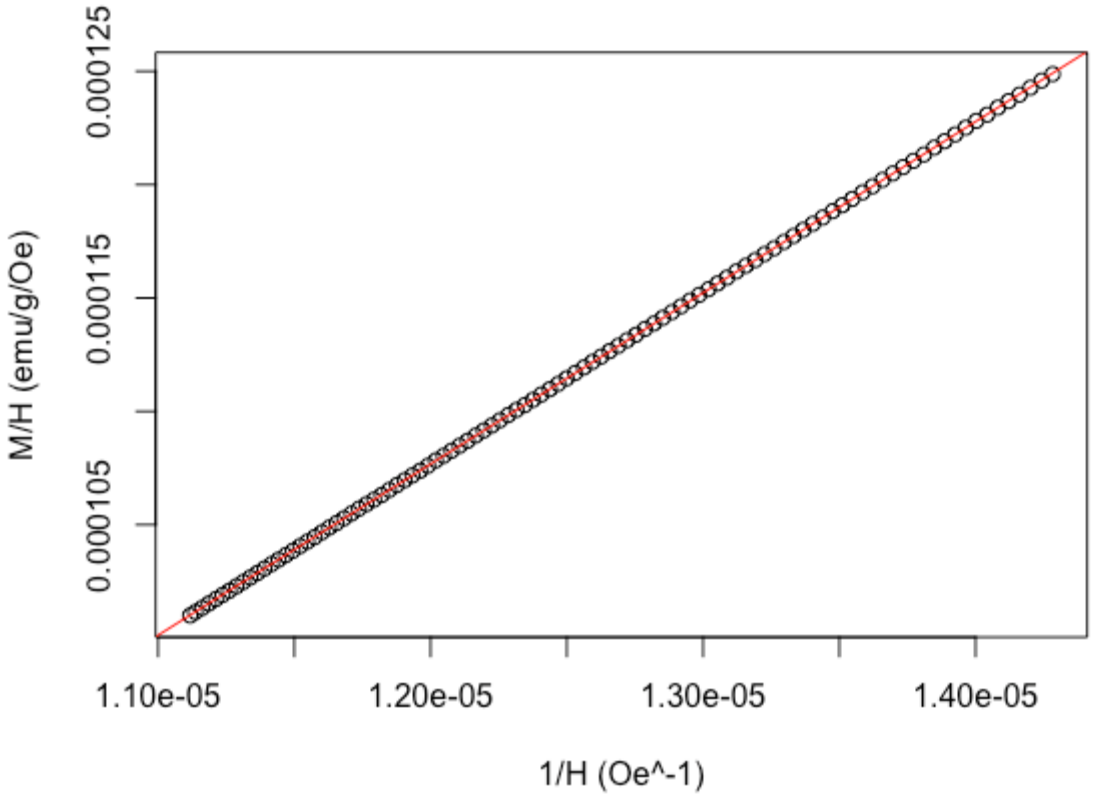

Figure S13. Magnetization *versus* 1/*H* up to 9 T for core-shell nanoparticles. Experimental points are fitted (red line) according to the Honda-Owen approach: $M/H = M_s/H + X$. M_s and X are then evaluated to 7.552 emu g^{-1} and 1.704846e-05 emu g^{-1} Oe^{-1}. Note that $X > 0$ precludes occurrence of diamagnetic contribution that may have occurred from bulk CoSi impurities. The magnetization curve Figure 7b and the data shown in Figure S13 indicate than the signal is a combination of a ferromagnetic component (S-shape of the magnetization curve and saturation at high field) and a linear term, $X*H$, which amounts at 20 % of the saturation magnetization at 9 T. This last contribution may account for paramagnetic species or for weakly interactions spins.

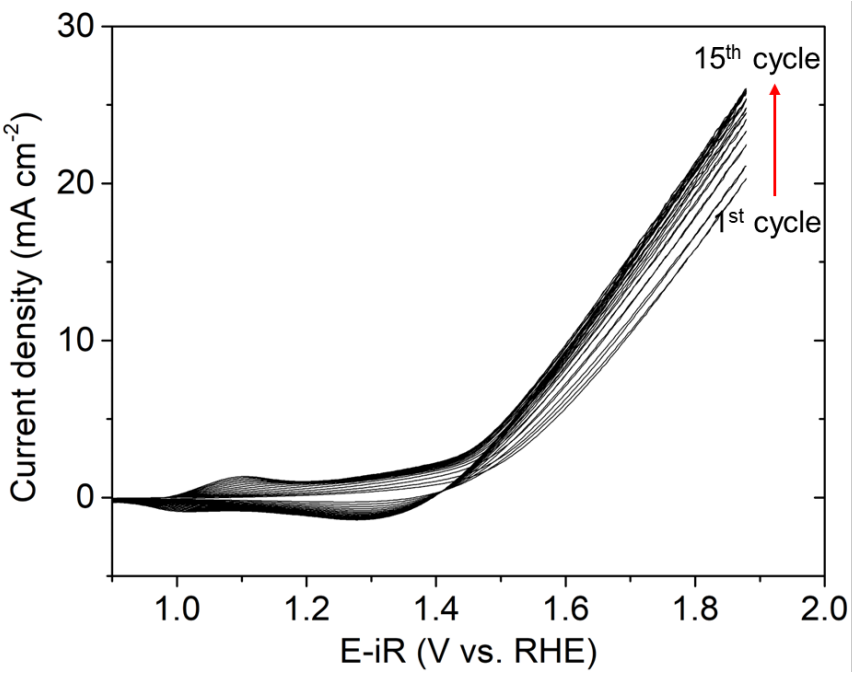

Figure S14. CVs of homogeneous CoSi nanoparticles in an aqueous O_2-saturated 0.1 M KOH electrolyte.

Table S4. Normalized OER electrocatalytic activity and stability of some previously reported cobalt-p-block element compounds electrocatalysts in 0.1 M KOH on a glassy carbon substrate.

Catalyst	Loading amount (mg cm^{-2})	Overpotential (mV) @10mA cm^{-2}	Overpotential (mV) @40mA cm^{-2} g_{Co}^{-1}	Stability (h)	Ref.
Core-shell CoSi	0.17	440	270	15 h	This work
Homogeneous CoSi	0.17	370	240	15 h	This work
Amorphous Co_2B	0.21	380	370	60 h	[24]
$CoSe_2$	0.20	484	420	/	[25]
CoB	0.21	370	390	51 h	[26]
Co_2B	0.20	405	360	1000 cycles	[27]

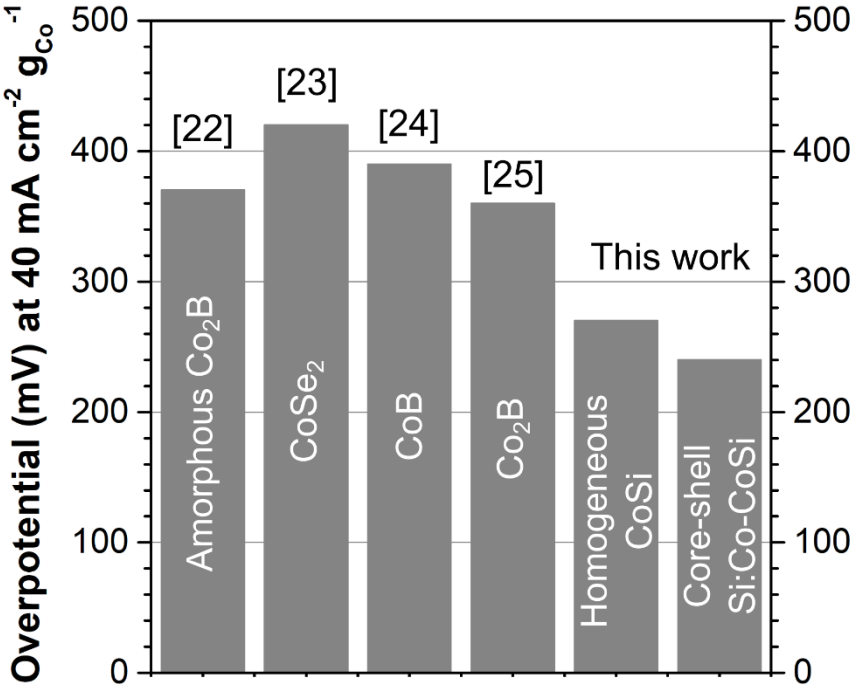

Figure S15. Normalized OER overpotentials for non-oxide precatalysts based on cobalt and p-block elements, taken from Table S3.

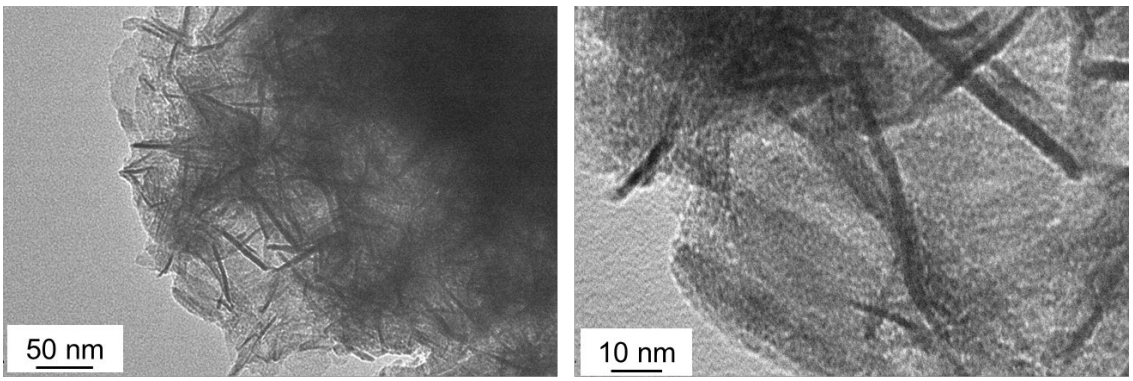

Figure S16. TEM images of the homogeneous CoSi nanoparticles after 15 h CP at 10 mA cm^{-2}.

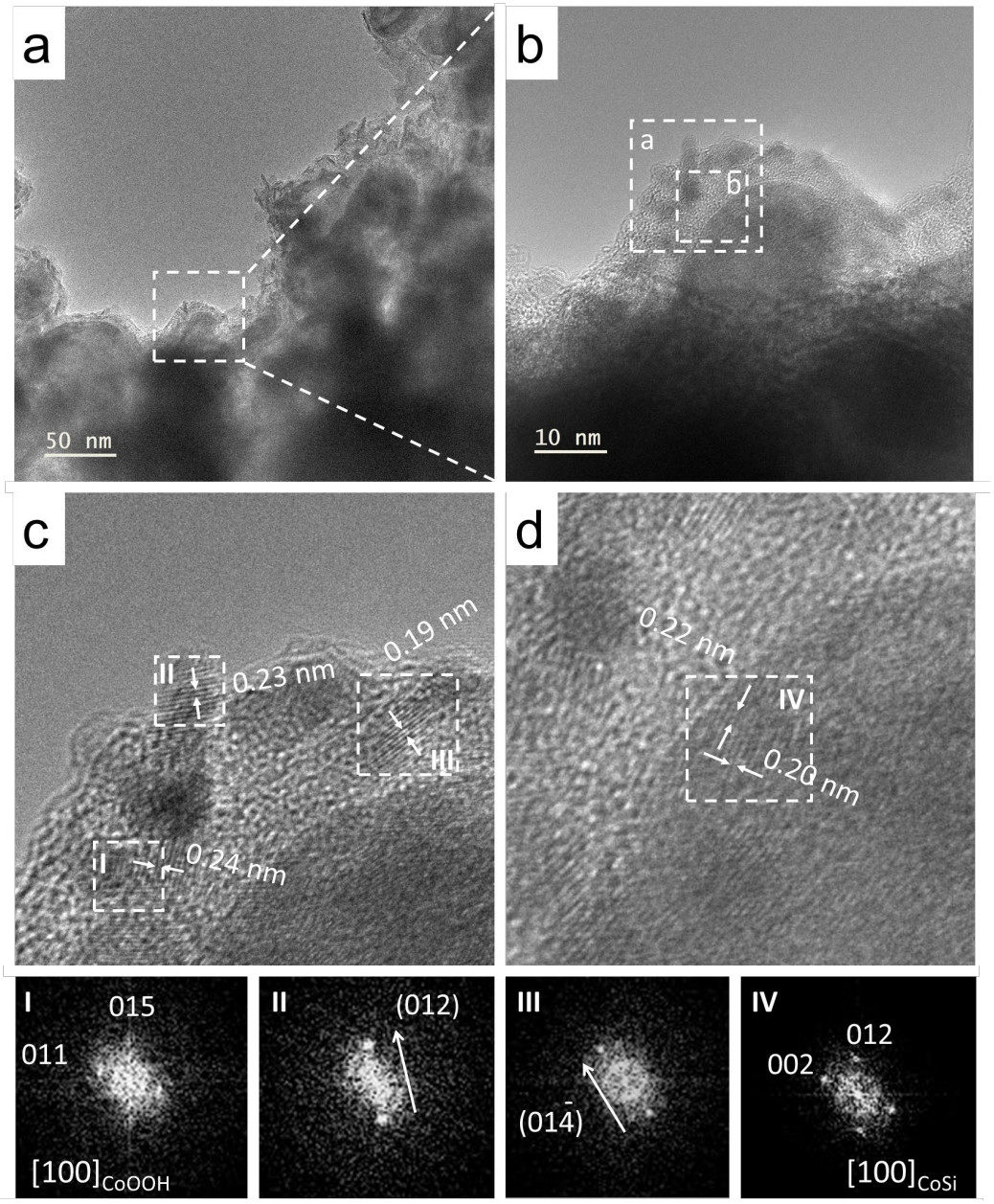

Figure S17. (a, b) TEM and (c, d) HRTEM images of CoSi nanoparticles after 15 h CP at 10 mA cm^{-2}. The FFTs shown in (I-IV) correspond to the areas delimited in (c) and (d) and are indexed along the CoOOH structure (*R-3m*, a: 2.8510 Å, *c*: 13.1500 Å). These images highlight poorly crystalline features that are related to the CoOOH structure.

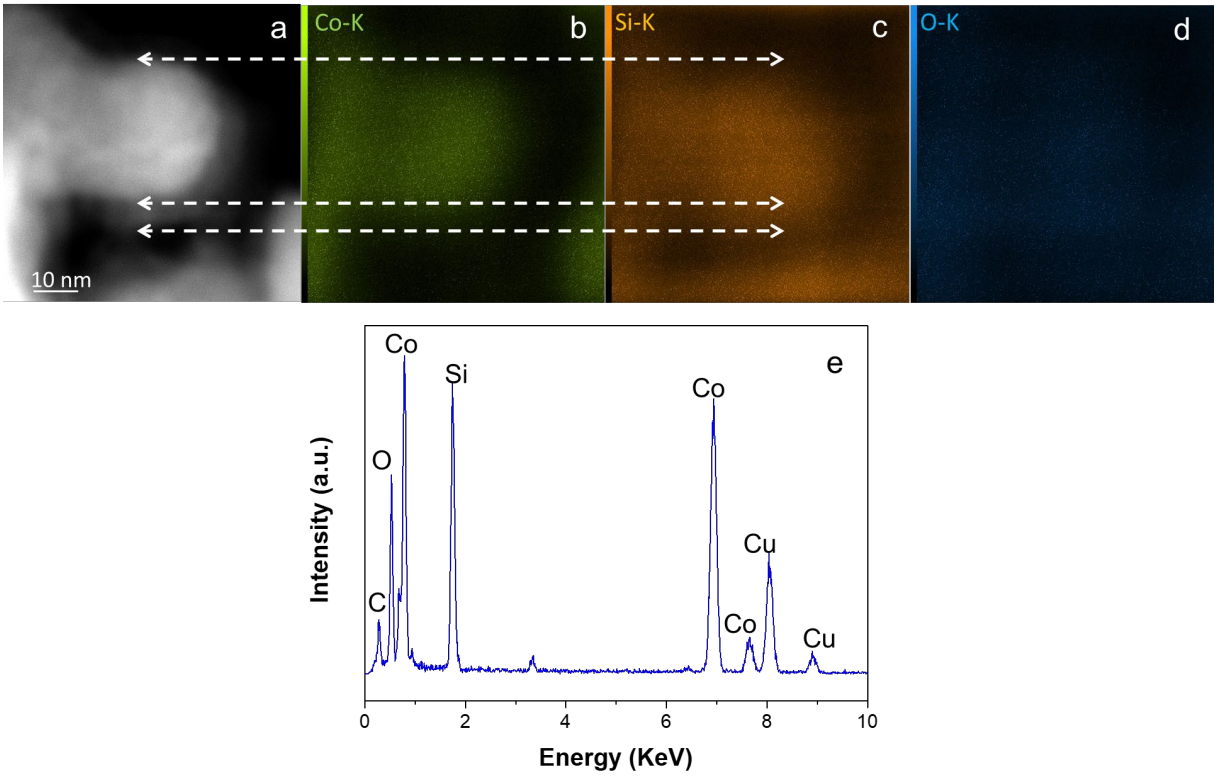

Figure S18. (a) STEM-HAADF and (b-d) STEM-EDS chemical maps of CoSi nanoparticles after 15 h CP at 10 mA cm^{-2}. (b) Co K-, (c) Si K-, and (d) O K-edges. (e) EDS sum spectrum recorded by STEM-EDS in the (a) area. The white arrows indicate areas where Si is detected out of the CoSi core, corresponding to the outer layer, hardly visible by HAADF detection due to low electron density, but better visualized by TEM in **Figure S16**.

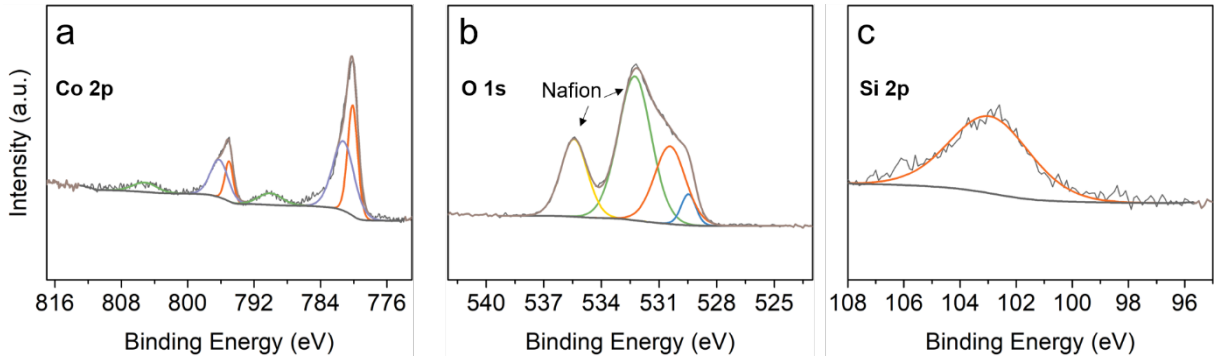

Figure S19. XPS of the core-shell nanoparticles after 15 h of OER at 10 mA cm^{-2}: (a) Co 2p, (b) O 1s, and (c) Si 2p regions. In (b), the Nafion® peaks are identified according to the literature.[21] A shift of the Co $2p_{3/2}$ signal to high binding energy compared to the initial material (**Figure S10**) is observed. The deconvoluted peaks at 780.1 eV and 781.2 eV and the satellite features indicate the presence of Co^{3+}, which corresponds to CoOOH and/or Co_3O_4.[28–31] In the O 1s region, the peak at the lowest binding energy 529.5 eV is attributed to cobalt oxide. The component at 530.5 eV can be assigned to typical non-stoichiometric oxygen in spinel (Co_3O_4) or cobalt hydroxide.[21,32] The Si 2p region shows a peak at 102.9 eV, shifted to lower energy compared to the pristine sample. It can be attributed to Si oxoanions,[33] presumably in the interlayer regions of cobalt oxide/(oxyhydroxide), which may assist the formation of the layered structure.[34]

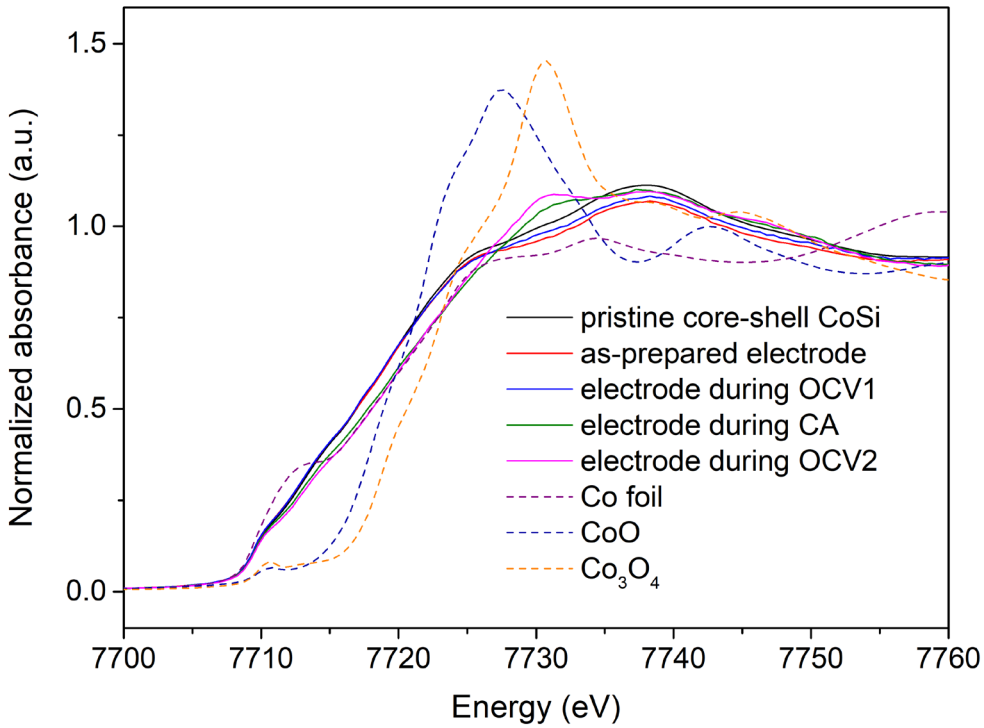

Figure S20. XANES spectra at the Co-K edge of pelletized sample and XANES spectra recorded *operando* for core-shell nanoparticles.

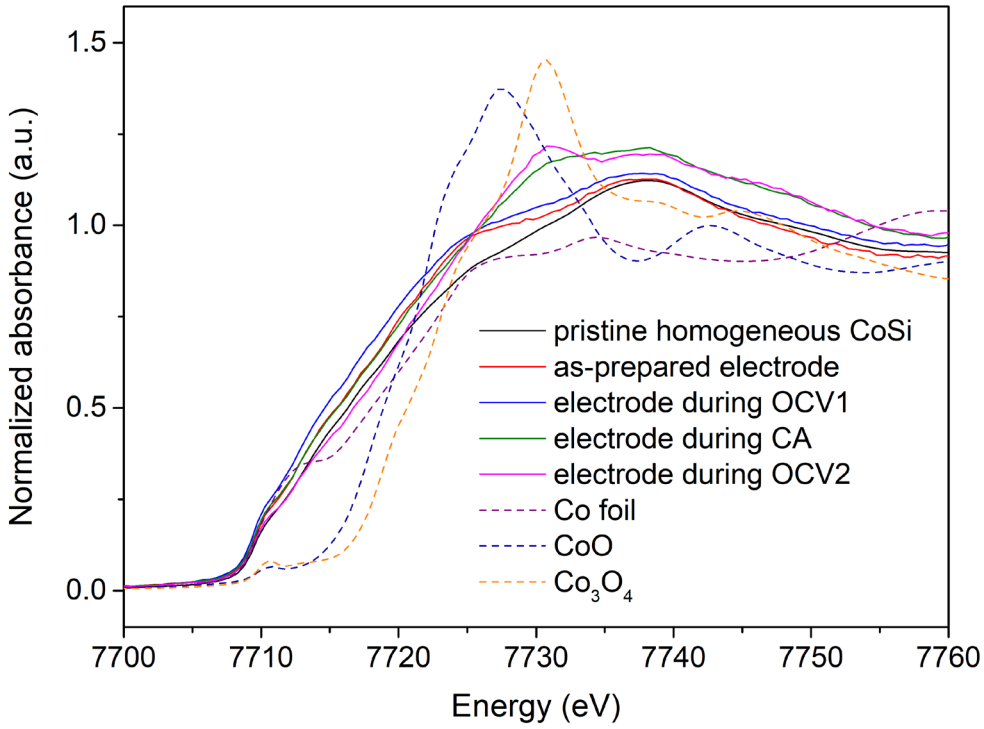

Figure S21. XANES spectra at the Co-K edge of pelletized sample and XANES spectra recorded *operando* for homogeneous CoSi nanoparticles.

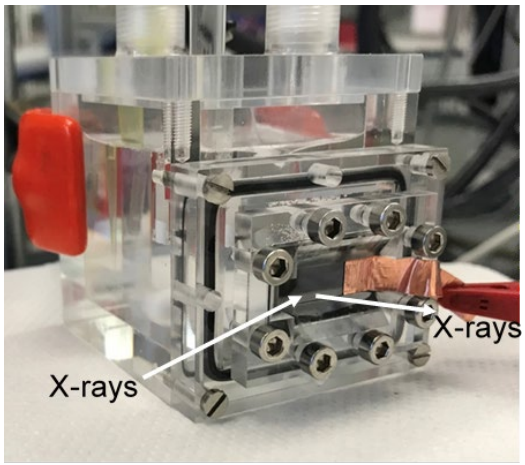

Figure S22. Custom-made electrochemical cell of three-electrode configuration for *operando* XAS analysis.

Table S5. LCF factors, corresponding to mol. contents, for homogeneous CoSi nanoparticles. The CoSi content is evaluated by using the XAS spectrum of the pristine homogeneous sample (**Figures 5e**, **S21**).

	CoSi	CoO	$Co(OH)_2$	Co_3O_4	Chi-square
As prepared electrode	0.943	0.057	0	0	0.119
OCV1 merged spectrum	0.978	0	0.022	0	0.190
CA merged spectrum	0.892	0	0	0.108	0.118
OCV2 merged spectrum	0.772	0	0	0.228	0.034
CA scan1	0.912	0	0	0	0.187
CA scan2	0.909	0	0	0	0.128
CA scan3	0.899	0	0	0	0.107
CA scan4	0.885	0	0	0	0.085
CA scan5	0.860	0	0	0	0.069

Table S6. LCF factors, corresponding to mol. contents, for core-shell nanoparticles. The CoSi content is evaluated by using the XAS spectrum of the pristine homogeneous CoSi sample (**Figures 5e**, **S21**).

	CoSi	CoO	$Co(OH)_2$	Co_3O_4	Chi-square
As prepared electrode	0.997	0.003	0	0	0.019
OCV1 merged spectrum	1.000	0	0	0	0.011
CA merged spectrum	0.870	0	0	0.130	0.045
OCV2 merged spectrum	0.792	0	0	0.208	0.034
CA scan1	0.897	0	0	0.103	0.029
CA scan2	0.848	0	0	0.152	0.062
CA scan3	0.840	0	0	0.160	0.068

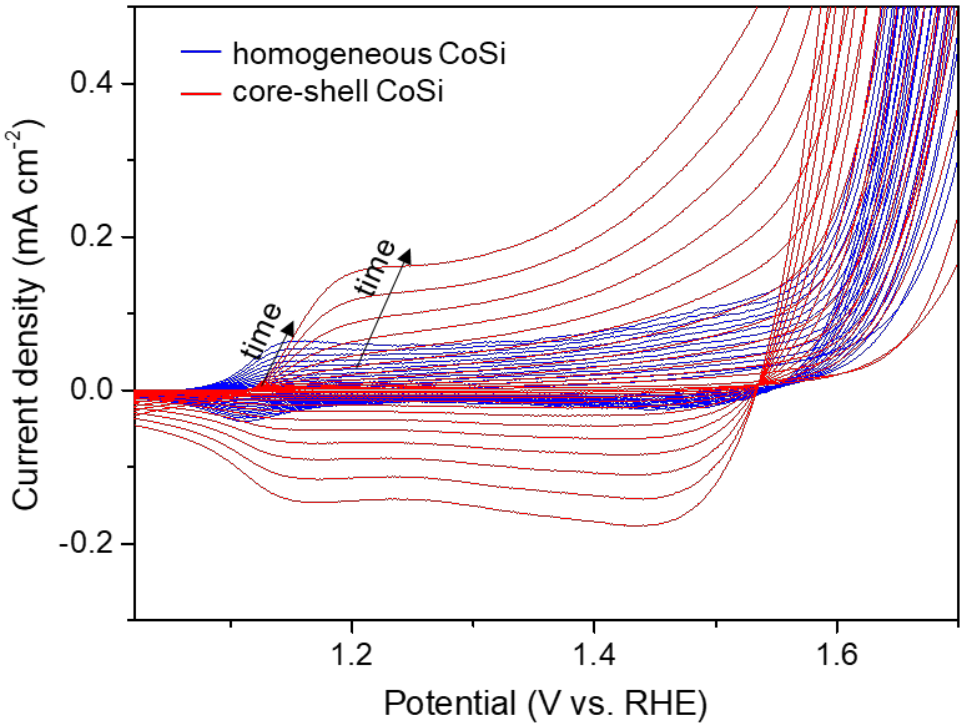

Figure S23. CVs of homogeneous CoSi and core-shell CoSi nanoparticles measured during *operando* XAS in an aqueous O_2-saturated 0.1 M KOH electrolyte.

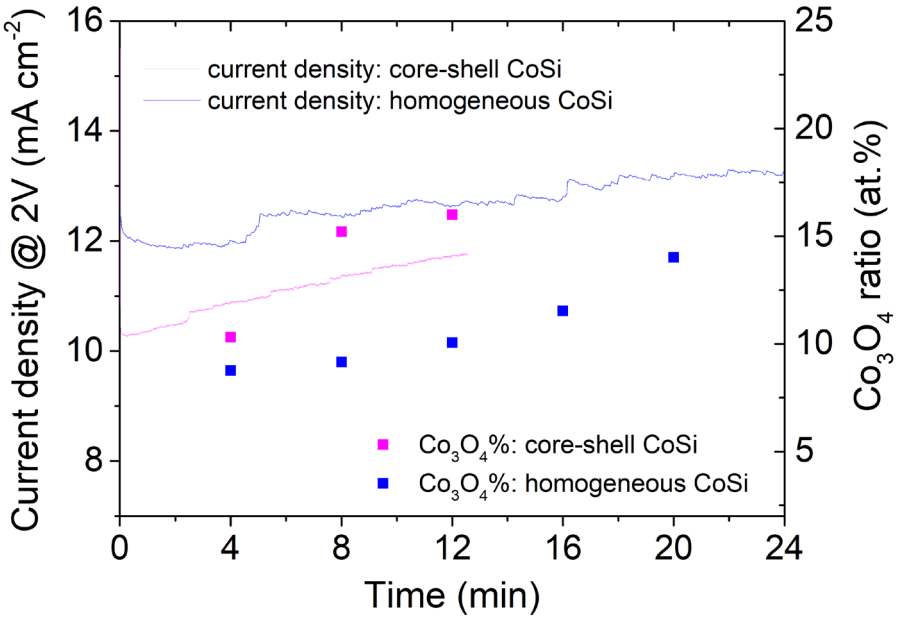

Figure S24. The evolution of the ratio of cobalt oxide/oxyhydroxide from silicide nanoparticles during chronoamperometry at 2.0 V / RHE, based on the LCF of XAS spectra by using Co_3O_4 as a reference, as reported in **Tables S5** and **S6**.

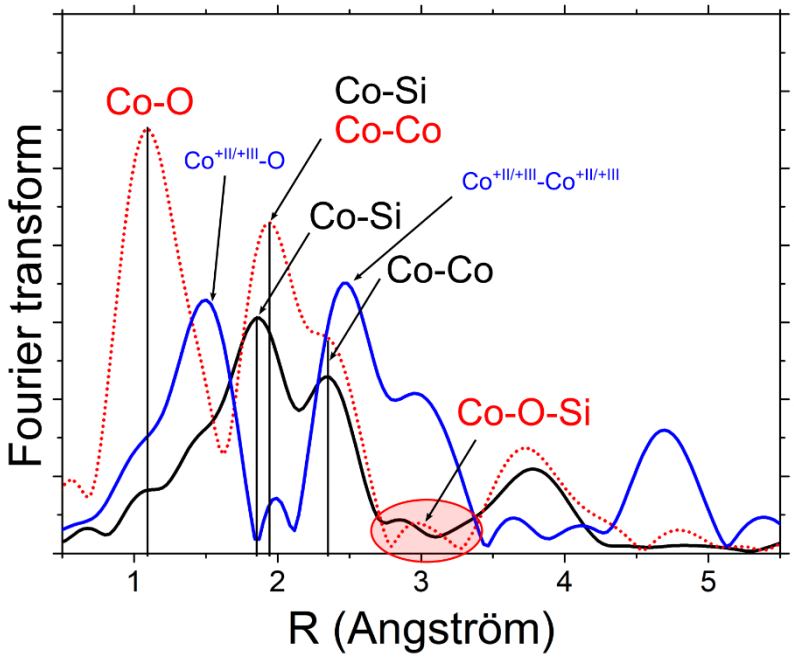

Figure S25. Co K-edge EXAFS of (black) the pristine CoSi powder, (red) the material analyzed *in situ* during OER electrocatalysis (chronoamperometry at -2 V vs. RHE), and (blue) a Co_3O_4 reference. No phase-shift correction was applied, so that the distance measured is an apparent distance. Black labeled Co-Si and Co-Co shells correspond to the CoSi structure. Red labeled Co-O, Co-Co and Co-O-Si shells correspond to distances measured in the operating material and that can be ascribed to CoO_6 octahedra and SiO_4 tetrahedra connected by vertices, as in a cobalt phyllosilicate.[35]

Supporting references

(1) Lucas, G.; Burdet, P.; Cantoni, M.; Hébert, C. Multivariate Statistical Analysis as a Tool for the Segmentation of 3D Spectral Data. *Micron* **2013**, *52–53*, 49–56. https://doi.org/https://doi.org/10.1016/j.micron.2013.08.005.

(2) Sode, J. Spectroscopy and Modelling of Catalyst Nanoparticles Using STEM-EELS, University of Oxford, 2021.

(3) Zhao, Y.; Feltes, T. E.; Regalbuto, J. R.; Meyer, R. J.; Klie, R. F. In Situ Electron Energy Loss Spectroscopy Study of Metallic Co and Co Oxides. *J. Appl. Phys.* **2010**, *108* (6), 63704. https://doi.org/10.1063/1.3482013.

(4) Yu-Zhang, K.; Imhoff, D.; Leprince-Wang, Y.; Roy, E.; Zhou, S. M.; Chien, C. L. Multi-Scale Analysis of the Nanostructured Granular Solid CoO–Ag by TEM and EELS. *Acta Mater.* **2003**, *51* (4), 1157–1166. https://doi.org/https://doi.org/10.1016/S1359-6454(02)00520-7.

(5) Juhás, P.; Davis, T.; Farrow, C. L.; Billinge, S. J. L. PDFgetX3: A Rapid and Highly Automatable Program for Processing Powder Diffraction Data into Total Scattering Pair Distribution Functions. *J. Appl. Crystallogr.* **2013**, *46* (2), 560–566. https://doi.org/10.1107/S0021889813005190.

(6) Farrow, C. L.; Juhas, P.; Liu, J. W.; Bryndin, D.; Boin, E. S.; Bloch, J.; Proffen, T.; Billinge, S. J. L. PDFfit2 and PDFgui: Computer Programs for Studying Nanostructure in Crystals. *J. Phys. Cond. Matter* **2007**, *19* (33). https://doi.org/10.1088/0953-8984/19/33/335219.

(7) Terban, M. W.; Billinge, S. J. L. Structural Analysis of Molecular Materials Using the Pair Distribution Function. *Chem. Rev.* **2022**, 122 (1), 1208–1272. https://doi.org/10.1021/acs.chemrev.1c00237.

(8) Ahn, C. C.; Krivanek, O. L.; Burgner, R. P.; Disko, M. M.; Swann, P. R. EELS Atlas : A Reference Collection of Electron Energy Loss Spectra Covering All Stable Elements; Gatan, Inc., Warrendale, Pa., 1983.

(9) Van Campen, D. G.; Klebanoff, L. E. Spin-Resolved and High-Energy-Resolution XPS Studies of the 3s and 2s Levels of Metallic Cobalt. *Phys. Rev. B* **1994**, *49* (3), 2040–2046. https://doi.org/10.1103/PhysRevB.49.2040.

(10) Rakityanskaya, I. L.; Shein, A. B. Anodic Behavior of Iron, Cobalt, and Nickel Silicides in Alkaline Electrolytes. *Russ. J. Electrochem.* **2006**, *42* (11), 1208–1212. https://doi.org/10.1134/S1023193506110073.

(11) Zieschang, A. M.; Bocarsly, J. D.; Schuch, J.; Reichel, C. V.; Kaiser, B.; Jaegermann, W.; Seshadri, R.; Albert, B. Magnetic and Electrocatalytic Properties of Nanoscale Cobalt Boride, Co_3B. *Inorg. Chem.* **2019**, *58* (24), 16609–16617. https://doi.org/10.1021/acs.inorgchem.9b02617.

(12) Hao, S. M.; Yu, M. Y.; Zhang, Y. J.; Abdelkrim, Y.; Qu, J. Hierarchical Mesoporous Cobalt Silicate Architectures as High-Performance Sulfate-Radical-Based Advanced Oxidization Catalysts. *J Coll. Interf. Sci.* **2019**, *545*, 128–137. https://doi.org/10.1016/j.jcis.2019.03.017.

(13) García-Méndez, M.; Castillón, F. F.; Hirata, G. A.; Farías, M. H.; Beamson, G. XPS and HRTEM Characterization of Cobalt-Nickel Silicide Thin Films. *Appl. Surf. Sci.* **2000**, *161* (1), 61–73. https://doi.org/10.1016/S0169-4332(00)00122-7.

(14) Kichigin, V. I.; Shein, A. B. Anodic Behavior of Cobalt Silicides in Potassium Hydroxide Solutions. *Protection Met. Phys. Chem. Surf.* **2013**, *49* (3), 336–343. https://doi.org/10.1134/S2070205113030106.

(15) Hao, S. M.; Yu, M. Y.; Zhang, Y. J.; Abdelkrim, Y.; Qu, J. Hierarchical Mesoporous Cobalt Silicate Architectures as High-Performance Sulfate-Radical-Based Advanced Oxidization Catalysts. *J Coll. Interf. Sci* **2019**, *545*, 128–137. https://doi.org/10.1016/j.jcis.2019.03.017.

(16) Filipponi, A.; Di Cicco, A.; Natoli, C. R. X-Ray-Absorption Spectroscopy and n-Body Distribution Functions in Condensed Matter. I. Theory. *Phys. Rev. B* **1995**, *52* (21), 15122–15134. https://doi.org/10.1103/PhysRevB.52.15122.

(17) Filipponi, A.; Di Cicco, A. X-Ray-Absorption Spectroscopy and n-Body Distribution Functions in Condensed Matter. II. Data Analysis and Applications. *Phys. Rev. B* **1995**, *52* (21), 15135–15149. https://doi.org/10.1103/PhysRevB.52.15135.

(18) Seo, K.; Varadwaj, K. S. K.; Mohanty, P.; Lee, S.; Jo, Y.; Jung, M. H.; Kim, J.; Kim, B. Magnetic Properties of Single-Crystalline CoSi Nanowires. *Nano Lett.* **2007**, *7* (5), 1240–1245. https://doi.org/10.1021/nl070113h.

(19) Gomoyunova, M. V.; Grebenyuk, G. S.; Pronin, I. I.; Solov'ev, S. M.; Vilkov, O. Y.; Vyalykh, D. V. Formation and Magnetic Properties of the Silicon-Cobalt Interface. *Phys. Solid State* **2013**, *55* (2), 437–442. https://doi.org/10.1134/S1063783413020091.

(20) Stishov, S. M.; Petrova, A. E.; Sidorov, V. A.; Krasnorussky, V. N.; Menzel, D. Self-Doping Effects in Cobalt Silicide CoSi: Electrical, Magnetic, Elastic, and Thermodynamic Properties. *Phys. Rev. B* **2012**, *86* (6), 1–5. https://doi.org/10.1103/PhysRevB.86.064433.

(21) Zieschang, A. M.; Bocarsly, J. D.; Schuch, J.; Reichel, C. V.; Kaiser, B.; Jaegermann, W.; Seshadri, R.; Albert, B. Magnetic and Electrocatalytic Properties of Nanoscale Cobalt Boride, Co_3B. *Inorg. Chem.* **2019**, *58* (24), 16609–16617. https://doi.org/10.1021/acs.inorgchem.9b02617.

(22) Osuna, J.; De Caro, D.; Amiens, C.; Chaudret, B.; Snoeck, E.; Respaud, M.; Broto, J. M.; Fert, A. Synthesis, Characterization, and Magnetic Properties of Cobalt Nanoparticles from an Organometallic Precursor. *J. Phys. Chem.* **1996**, *100* (35), 14571–14574. https://doi.org/10.1021/jp961086e.

(23) Nishikawa, M.; Kita, E.; Erata, T.; Tasaki, A. Enhanced Magnetization in Co/MgO Multilayer Thin Films. *J. Magn. Magn. Mater.* **1993**, *126* (1–3), 303–306. https://doi.org/10.1016/0304-8853(93)90609-6.

(24) Masa, J.; Weide, P.; Peeters, D.; Sinev, I.; Xia, W.; Sun, Z.; Somsen, C.; Muhler, M.; Schuhmann, W. Amorphous Cobalt Boride (Co_2B) as a Highly Efficient Nonprecious Catalyst for Electrochemical Water Splitting: Oxygen and Hydrogen Evolution. *Adv. Ener. Mater.* **2016**, *6* (6), 1–10. https://doi.org/10.1002/aenm.201502313.

(25) Gao, M.; Cao, X.; Gao, Q.; Xu, Y.; Zheng, Y.; Jiang, J.; Yu, S. Nitrogen-Doped Graphene Supported CoSe2 Nanobelt Composite Catalyst for Efficient Water Oxidation. *ACS Nano* **2014**, No. 4, 3970–3978.

(26) Elumeeva, K.; Masa, J.; Medina, D.; Ventosa, E.; Seisel, S.; Kayran, Y. U.; Genç, A.; Bobrowski, T.; Weide, P.; Arbiol, J.; Muhler, M.; Schuhmann, W. Cobalt Boride Modified with N-Doped Carbon Nanotubes as a High-Performance Bifunctional Oxygen Electrocatalyst. *J. Mater. Chem. A* **2017**, *5* (40), 21122–21129. https://doi.org/10.1039/c7ta06995b.

(27) Ma, X.; Wen, J.; Zhang, S.; Yuan, H.; Li, K.; Yan, F.; Zhang, X.; Chen, Y. Crystal Co_xB (x = 1-3) Synthesized by a Ball-Milling Method as High-Performance Electrocatalysts for the Oxygen Evolution Reaction. *ACS Sustain. Chem. Eng.* **2017**, *5* (11), 10266–10274. https://doi.org/10.1021/acssuschemeng.7b02281.

(28) Yang, J.; Liu, H.; Martens, W. N.; Frost, R. L. Synthesis and Characterization of Cobalt Hydroxide, Cobalt Oxyhydroxide, and Cobalt Oxide Nanodiscs. *J. Phys. Chem. C* **2010**, *114* (1), 111–119. https://doi.org/10.1021/jp908548f.

(29) Biesinger, M. C.; Payne, B. P.; Grosvenor, A. P.; Lau, L. W. M.; Gerson, A. R.; Smart, R. S. C. Resolving Surface Chemical States in XPS Analysis of First Row Transition Metals, Oxides and Hydroxides: Cr, Mn, Fe, Co and Ni. *Appl. Surf. Sci.* **2011**, *257* (7), 2717–2730. https://doi.org/10.1016/j.apsusc.2010.10.051.

(30) Weidler, N.; Paulus, S.; Schuch, J.; Klett, J.; Hoch, S.; Stenner, P.; Maljusch, A.; Brötz, J.; Wittich, C.; Kaiser, B.; Jaegermann, W. CoO_x Thin Film Deposited by CVD as Efficient Water Oxidation Catalyst: Change of Oxidation State in XPS and Its Correlation to Electrochemical Activity. *Phys. Chem. Chem. Phys.* **2016**, *18* (16), 10708–10718. https://doi.org/10.1039/c5cp05691h.

(31) Qiao, L.; Xiao, H. Y.; Meyer, H. M.; Sun, J. N.; Rouleau, C. M.; Puretzky, A. A.; Geohegan, D. B.; Ivanov, I. N.; Yoon, M.; Weber, W. J.; Biegalski, M. D. Nature of the Band Gap and Origin of the Electro-/Photo-Activity of Co_3O_4. *J. Mater. Chem. C* **2013**, *1* (31), 4628–4633. https://doi.org/10.1039/c3tc30861h.

(32) Yang, J.; Liu, H.; Martens, W. N.; Frost, R. L. Synthesis and Characterization of Cobalt Hydroxide, Cobalt Oxyhydroxide, and Cobalt Oxide Nanodiscs. *J. Phys. Chem. C* **2010**, *114* (1), 111–119. https://doi.org/10.1021/jp908548f.

(33) Shen, Y.; Cao, Z.; Wu, Y.; Cheng, Y.; Xue, H.; Zou, Y.; Liu, G.; Yin, D.; Cavallo, L.; Wang, L.; Ming, J. Catalysis of Silica-Based Anode (de-)Lithiation: Compositional Design within a Hollow Structure for Accelerated Conversion Reaction Kinetics. *J. Mater. Chem. A* **2020**, *8* (25), 12306–12313. https://doi.org/10.1039/d0ta01671c.

(34) Masa, J.; Schuhmann, W. The Role of Non-Metallic and Metalloid Elements on the Electrocatalytic Activity of Cobalt and Nickel Catalysts for the Oxygen Evolution Reaction. *ChemCatChem* **2019**, *11* (24), 5842–5854. https://doi.org/10.1002/cctc.201901151.

(35) Kim, J. S.; Park, I.; Jeong, E. S.; Jin, K.; Seong, W. M.; Yoon, G.; Kim, H.; Kim, B.; Nam, K. T.; Kang, K. Amorphous Cobalt Phyllosilicate with Layered Crystalline Motifs as Water Oxidation Catalyst. *Adv. Mater.* **2017**, *29* (21). https://doi.org/10.1002/adma.201606893.